Materials Characterization 221 (2025) 114745

Contents lists available at ScienceDirect

Materials Characterization

journal homepage: www.elsevier.com/locate/matchar

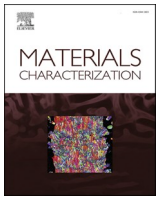

Three-dimensional analysis of the delta-ferrite to austenite phase transformation in an additively manufactured duplex stainless steel

X.Y. He [a], Z.P. Xu [b], G.S. Rohrer [b], C. Kong [c], S. Primig [a,*], N. Haghdadi [a,*]

[a] School of Materials Science & Engineering, UNSW Sydney, Sydney, NSW 2052, Australia
[b] Department of Materials Science and Engineering, Carnegie Mellon University, Pittsburgh, PA 15213-3890, USA
[c] Electron Microscope Unit, Mark Wainwright Analytical Centre, UNSW, Sydney, NSW 2052, Australia

ARTICLE INFO

Keywords:
Additive manufacturing
Duplex stainless steels
Phase transformation
3D-EBSD
Crystallography

ABSTRACT

A fundamental understanding of the δ-ferrite to austenite phase transformation and characteristics of the interfaces formed is currently lacking due to challenges in achieving fully ferritic starting microstructure during conventional processing. Here, a 2205 duplex stainless steel manufactured by laser powder bed fusion (LPBF) is used as a model system to reveal the fundamentals of the δ-ferrite to austenite phase transformation with the aid of three-dimensional electron backscattered diffraction (EBSD). A predominantly δ-ferritic non-equilibrium microstructure is obtained through the high cooling rate during LPBF. During a short thermal treatment of this starting microstructure, four distinct types of austenite (intergranular, instability-induced, sympathetic, and intragranular) are formed. The sympathetic and intragranular austenite present significantly higher area fractions of interfaces following the Kurdjumov-Sachs (K—S) or Nishiyama-Wassermann (N—W) orientation relationships (ORs) compared to intergranular austenite, owing to their different nucleation and growth mechanisms. The habit plane distributions of various interfaces reveal that ferrite and austenite terminate on (110) and (111) planes, respectively. Interestingly, the plane and curvature distributions do not always exhibit an inverse correlation in the sympathetic and intragranular transformation paths, while the non-K-S/N-W interfaces exhibit lower grain boundary curvatures compared to the K-S/N-W ones. This could be because the total energy minimization associated with phase transformation involves contributions from both the surface energy at grain boundaries and the elastic bulk energy. These new insights into the δ-ferrite to austenite transformation enable duplex microstructure design via additive manufacturing and subsequent post-processing to achieve superior properties.

1. Introduction

Additive manufacturing (AM) provides unparalleled opportunities to produce net-shaped or near net-shaped components with complex geometries [1,2]. However, the cyclic rapid heating and cooling as well as the highly localized melting and solidification during laser powder bed fusion (LPBF) lead to each material voxel experiencing complex thermal histories and steep thermal gradients [1,3]. This encourages the development of highly non-equilibrium as-LPBF microstructures with high dislocation densities [4,5]. The complexity of non-equilibrium microstructures increases in alloy grades that undergo subsequent solid-state phase transformations during and/or after AM, for example, steels that experience δ-ferrite to austenite and/or austenite to martensite/bainite/ferrite transformations [6–8] or titanium alloys that undergo β to α/α' transformations [9–11]. The formation of fine and complex morphologies such as Widmanstätten in steels and acicular laths in titanium alloys often involves protrusions inclined and/or interconnected in three dimensions (3D). While the morphology and crystallography of the fine α phase in a Ti-6Al-4V has been extensively studied in 3D to infer phase transformation mechanisms [9–11], available 3D investigations of multi-phase steels remain limited to reports on their morphology only, without orientation data [12]. Studies on the crystallography and grain boundary characteristics in multi-phase steels have so far been conducted using two-dimensional (2D) microscopy [6,13–15]. Despite valuable insights drawn from 2D analyses, a lack of 3D orientation data captured on multi-phase microstructures hinders the unambiguous categorization of different phase transformation mechanisms and, hence, there remain knowledge gaps in the understanding of the driving

* Corresponding authors.
E-mail addresses: s.primig@unsw.edu.au (S. Primig), nima.haghdadi@unsw.edu.au (N. Haghdadi).

https://doi.org/10.1016/j.matchar.2025.114745
Received 10 November 2024; Received in revised form 19 December 2024; Accepted 11 January 2025
Available online 13 January 2025

forces of the different phase transformation pathways. The microstructural features of complex dual-phase materials cannot be comprehensively analysed from any single 2D slice, but requires a 3D approach providing information on not only the microstructural morphology but also the crystallographic information of grains and interfaces.

In recent years, 3D microstructural characterization techniques have been frequently applied to single phase metallic and ceramic polycrystals [9–11,16–19] to quantitatively measure the microstructural characteristics that could not be fully understood from 2D characterization alone. In particular, grain boundary plane and curvature distributions have been quantified using 3D orientation data [17,20]. Grain boundary microstructures are recognized to vastly affect materials properties including strength [21], corrosion behaviour [22], and electrical resistance [23]. Recent advancements in serial sectioning using a Xe^+ plasma focused ion beam (PFIB) scanning electron microscope enables a relatively fast acquisition of electron backscattered diffraction (EBSD) maps on parallel layers with high spatial resolution (~50 nm) [24] and relatively large volumes (~40,000 μm^3 in Ref. [25] and ~690,000 μm^3 in the current study). This 3D characterization technique is capable of collecting significantly larger volumes than its Ga-ion counterpart in the same time [17], while achieving finer step sizes (higher resolution) than its tri-beam counterpart [26]. These unique features make it suitable for capturing fine and complex microstructural features such as the Widmanstätten austenite in stainless steels and acicular α/α' laths in titanium alloys.

Duplex stainless steels (DSSs) possess remarkable mechanical (strength, toughness) and corrosion properties achieved via the synergy of the properties of δ-ferrite (referred to as ferrite in the following) and austenite [27]. They are therefore broadly used in harsh conditions, including in desalination plants, oil & gas infrastructures, paper & pulp industries, and marine applications [28]. In addition to their technological significance, DSS can be considered as a model system [13] for research concerning the ferrite to austenite phase transformation to reveal the mechanisms driving the various transformation pathways and interface characteristics. This is important as ferrite-austenite interface characteristics, that are controlled by the phase transformation route, are the dominating factors in the superplasticity [29], microdeformation [30], precipitation behaviour [15], and restoration [14] of these classes of steels. The significant grain refinement and multiple austenite deformation mechanisms achieved in the post-LPBF thermally treated DSS 2205 that contribute to its optimal mechanical properties have also been associated with the ferrite to austenite phase transformation [27]. The extent of elemental segregation at the interphase boundaries, cell structures and grain boundaries in DSS 2205 processed via LPBF have been studied using transmission electron microscope and atom probe tomography [6,31,32]. Compared to the as-built austenite content of >20 % in DSSs fabricated using directed energy deposition [33–36], austenite bypassing leading to nearly no austenite formation in the as-built DSSs processed by LPBF [6,7,27,37]. There is a lack of knowledge regarding the subsequent solid-state phase transformation from ferrite to austenite in LPBF manufactured DSSs, which is mainly achieved via post-process thermal treatment.

To comprehensively study the interfaces between two neighbouring crystals, in addition to the lattice disorientation, the grain boundary plane and curvature distributions are required. Recent developments in integrating 3D-EBSD data with interface characteristics analysis have enabled the measurement of all parameters of the interfaces in various polycrystalline materials. This approach has been successfully implemented for a wide variety of single-phase microstructures [9–11,16–19]. However, a comprehensive 3D analysis of the interfaces developed during a body centred cubic (BCC) to face centred cubic (FCC) transformation is still lacking in the literature. In particular, there has been no study correlating such analysis with the microstructural evolution during AM and post-AM thermal treatments. Therefore, the goal of the current work is to unravel the influence of the phase transformation mechanisms on the austenite morphology and the characteristics of the interfaces developed during the ferrite to austenite phase transformation. We study an LPBF manufactured duplex stainless steel using a 3D orientation dataset collected via serial sectioning and EBSD. The main motivation is to provide new insights into how the non-equilibrium as-built microstructures obtained from AM impact the subsequent solid-state phase transformation and how the phase transformation pathway dictates the austenite morphology and ferrite-austenite interface characteristics. Considering the formerly established effects of austenite morphology and ferrite-austenite character on properties, such as deformation mechanisms [30], hot working process [14], and precipitation [15] in these types of steels, this investigation would ultimately guide the design of AM processing and thermal treatment towards engineering microstructure for superior properties.

2. Experimental

The DSS 2205 powder used was acquired from Sandvik Osprey Ltd., with an elemental composition of 22.60 Cr, 5.90 Ni, 1.10 Mn, 3.20 Mo, 0.60 Si, 0.02C, 0.02P, 0.01 S, 0.18 N (in wt%), and a balance of Fe. The powder particles were of mainly globular morphology and had particle diameters between 15 and 53 μm (measured by sieve and laser diffraction analyses). An SLM Solution 125^{HL} machine furnished with a 400 W continuous wavelength fibre laser was employed to print the samples, where an Ar shielding gas was applied to keep the O_2 content below 200 ppm. The printing parameters were 200 W laser power, 700 mm/s scanning speed, 30 μm layer thickness, 500 total layers, 60 μm hatch spacing, and a 67° incremental rotation between consecutive layers with a raster scan strategy (Fig. 1(a)). A 316 L stainless steel plate pre-heated to 200 °C served as the substrate. Cubic samples with a 15 mm edge length were printed (Fig. 1(b)). Based on our previous studies [6,37], a post-LPBF thermal treatment was implemented on selected samples at 1000 °C for 10 min in a tube furnace filled with Ar shielding gas, followed by water quenching to form a fine equilibrium microstructure.

The as-built DSS samples were investigated by 2D-EBSD on the x-z surface (Fig. 1(b)) within the central areas along the build direction (BD). The 2D-EBSD specimens were subjected to fine polishing with 0.04 μm OPU colloidal silica as the finishing step. Scanning transmission electron microscopy (STEM) specimens were extracted from the 2D-EBSD specimens using a standard plasma focused ion beam (FIB) lift-out method [38] on a Thermo Fisher Helios G4 Xe plasma FIB system. A JEOL 7001F scanning electron microscope equipped with a Hikari 31 Super EBSD Camera was used to conduct 2D-EBSD analysis, operating at 20 kV, 13 nA probe current, 6 × 6 binning configuration, and a step size of 1 μm. The TSL-OIM software was used for data acquisition and post-processing. STEM characterization of the as-built DSS specimens were conducted on a JEOL JEM-F200 (S)TEM, with a cold field emission gun operating at 200 kV.

Block-face serial sectioning was performed in a ThermoFisher Helios G4 PFIB Xe^+ DualBeam system to collect the 3D-EBSD dataset for the post-LPBF thermally treated DSS 2205. The sample was prepared and set up as described in Ref. [26]. The Aztec4.0 EBSD collection software and the Auto Slice and View software were used for operational control. Rocking milling was used to minimize curtaining effects. The slice thickness was 100 nm and the EBSD data was collected on every other slice with a step size of 200 nm. The 3D orientation map was developed from stacks of parallel 2D EBSD orientation maps. The volume of the collected dataset was ~100 × 75 × 92 μm^3 (Fig. 1(c)).

3D reconstruction and data analysis were conducted using the DREAM.3D software package [39] and the MTEX toolbox in Matlab [40]. Visualizations were realized using the ParaView software [41]. In general, the reconstruction process involved alignment, clean-up, segmentation, and meshing. After importing the data, voxels with too low (<20) or too high (>160) band contrast or non-zero error were cleaned up. Assigned by the Aztec4.0 EBSD collection software, band contrast is a metric that measures the quality of the Kikuchi patterns, and a non-zero error indicates that a voxel is unindexable. Next, sub-pixel

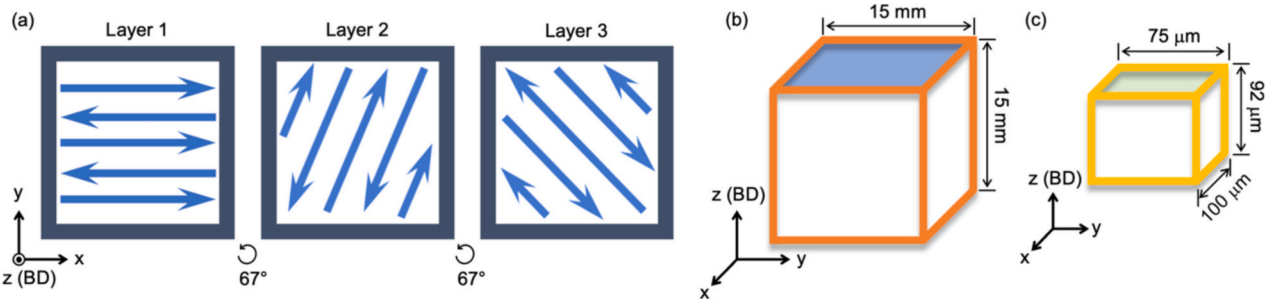

Fig. 1. Schematic view of (a) printing strategy with bi-directional scan and a 67° incremental rotation between consecutive layers, (b) cubic sample with dimensions and orientation, and (c) 3D-EBSD collection geometry and orientation.

misalignment between 2D slices was corrected by using centroid and misorientation based algorithms [42], where the misorientation tolerance was set to 0.5°. For grain segmentation within the 3D volume, each voxel orientation was compared to its neighbours and a unique grain identification (ID) number was assigned to each collection of voxels with an orientation difference $< 1°$. In addition, grains were required to have at least 10 voxels and two neighbouring grains. Implementing these conditions introduced gaps in the microstructure volume by groups with no more than 10 voxels and un-indexed voxels. These gaps were then removed by uniformly dilating neighbouring grains in DREAM.3D [39,43]. In the final step, the average orientation of all voxels in each grain was assigned to each voxel within the grain. Due to the cubic voxel geometry, stair-stepped boundaries and triple lines were created which had to be smoothed to properly extract grain boundary plane distributions and grain boundary curvature distributions. Since local curvatures are of interest in this study, the boundary must be represented as a surface comprised of discrete triangles. A quick surface meshing algorithm in DREAM.3D was employed to map the grain boundaries as triangular nets followed by a restricted Laplacian smoothing that generated smoothly curved grain boundaries. In total, the processed dataset contained around 69.6 million voxels and was segmented into 65,146 unique grains with 297,075 grain boundaries and 57,343,510 triangles.

Using the meshed 3D-EBSD data, the grain boundary (mean) curvature was measured locally for all triangles by applying the previously developed cubic-order algorithm detailed in Ref. [44] and implemented in DREAM.3D [39,45]. In this algorithm, a patch of contiguous triangles encompassing the triangle of interest is fit to a parabola. The crystallographic properties of the neighbourhood triangle patch which includes 2nd and 3rd nearest neighbours of the targeted triangle are known. The Weingarten matrix of this triangle patch can be obtained after applying a least-squares method to fit the parabola. The eigenvalues of the Weingarten matrix are the principal curvatures k_1 and k_2, and the triangle mean curvature is then $(k_1 + k_2)/2$, where a convex interface has a positive curvature and a concave one has a negative curvature. Here, only the absolute values of the triangle mean curvatures were considered for measurements of the grain boundary curvature distributions [20].

Once the 3D orientation data reconstruction is completed, the microstructure is comprised of discrete grains with unique ID numbers wrapped by a triangular mesh. Each triangle in the mesh is associated with information including the grain ID numbers on both sides, the grain orientations on both sides, the disorientation across the triangle, the triangle area, the surface normal, and the curvature. This facilitates the local mapping of these quantities and the definition of their distributions over volumetric, morphological, and crystallographic parameters. Since the microstructure in this study contains two different phases, the reconstructed boundaries/triangles were classified into three categories: ferrite-austenite, ferrite-ferrite, and austenite-austenite interfaces. Based on austenite morphology, the ferrite-austenite interfaces can be further categorized into interfaces corresponding to ferrite boundaries with intergranular austenite, sympathetic austenite, and intragranular austenite, respectively. Further analysis was then performed on each of these groups of interfaces to determine the grain boundary plane and curvature distributions using the methodology described in detail in Ref. [20]. The ferrite-austenite interfaces were processed differently owing to the existence of two distinct phases on each side of the interface. In the current work, the interphase plane character distribution for distinct phases was computed separately, representing the ferrite and austenite habit planes.

3. Results

3.1. Overall microstructures

Figure 2 demonstrates 2D views of the typical as-built microstructures of the LPBF DSS 2205, exhibiting non-equilibrium characteristics including an unbalanced phase fraction (Fig. 2(a)), columnar grain structures (Fig. 2(b)), and strong texture in BD (Fig. 2(c)). From the EBSD phase map in Fig. 2(a), ferrite is observed to be the main constituent coloured in red, occupying more than 98 % of the map area, with small austenite particles shown in green colour. The EBSD inverse pole figure (IPF) map along the Y-direction (out-of-page) in Fig. 2(b) shows columnar grain structures extending towards the BD. From the IPF map along the BD in Fig. 2(c), the mostly red colour indicates a strong ⟨001⟩//BD texture in ferrite formed due to the epitaxial growth and preferential grain growth orientation of <001> in BCC microstructures manufactured by LPBF [6]. The STEM micrograph along the ferrite [001] zone axis in Fig. 2(d) indicates high density of dislocations and spherical inclusions in the as-built ferrite grain. These spherical inclusions as pointed out by red arrows have been shown to be amorphous Si—O via STEM and energy-dispersive X-ray spectroscopy in our previous reports on the same DSS [6,27].

The as-built LPBF DSS 2205 was then subjected to a 1000 °C thermal treatment for 10 min. A volumetric view of the microstructure of the thermally treated LPBF DSS 2205 is presented as an EBSD phase map (Fig. 3(a)), IPF map along the Y direction (Fig. 3(b)), and IPF map along the BD (Fig. 3(c)), respectively. An equilibrium (~40 %/60 %) austenite/ferrite fraction is retrieved by the post-AM thermal treatment as seen in Fig. 3(a). In Fig. 3(c), ferrite displays a strong <001> texture along the BD, with austenite primarily seen to possess a ⟨101⟩ texture along the BD, implying potential existence of specific orientation relationships (ORs) between the two phases. Observing from the three outer surfaces of the collected data volume in Fig. 3(a) and (b), austenite can be seen to reside mainly along the ferrite-ferrite GBs with limited intragranular austenite islands detected at the ferrite grain interiors. It should be noted that some of these observed intragranular austenite might have nucleated on the GBs beneath the three outer surfaces, therefore, a 2D characterization might not be sufficient to correctly identify different types of austenite growth. This highlights the importance of studying the 3D orientation dataset in enabling the complete and unambiguous categorization of different types of austenite formed

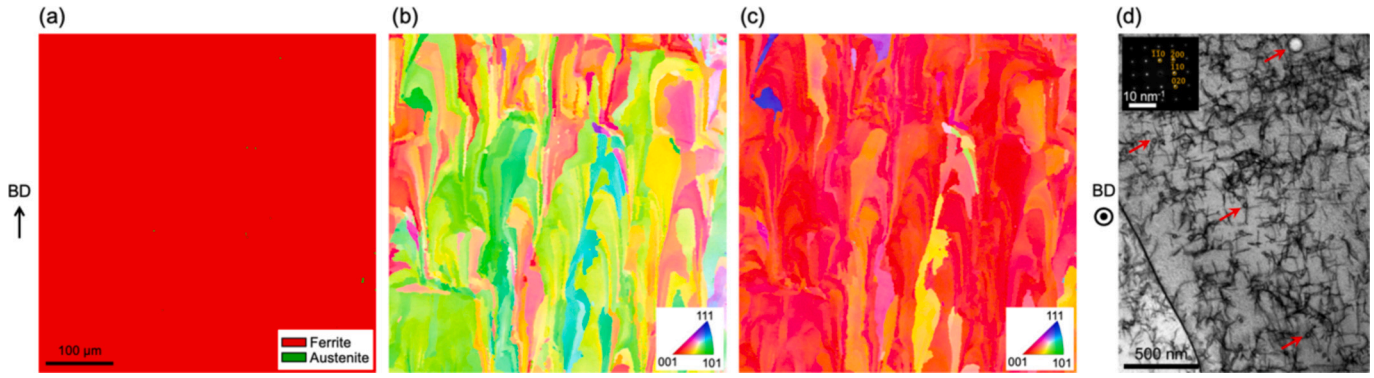

Fig. 2. Overall 2D views of the microstructure of the as-built LPBF DSS 2205. (a) EBSD phase map showing >98 % ferrite, BD is along the vertical direction. (b) EBSD IPF map along the Y-direction (out-of-page) displaying columnar grains of ferrite. (c) EBSD IPF map along the BD indicating a strong <001>//BD texture. (d) STEM micrograph along the ferrite [001] zone axis showing high density of dislocations and Si—O inclusions in the ferrite grain, red arrows point at examples of Si—O inclusions. (For interpretation of the references to colour in this figure legend, the reader is referred to the web version of this article.)

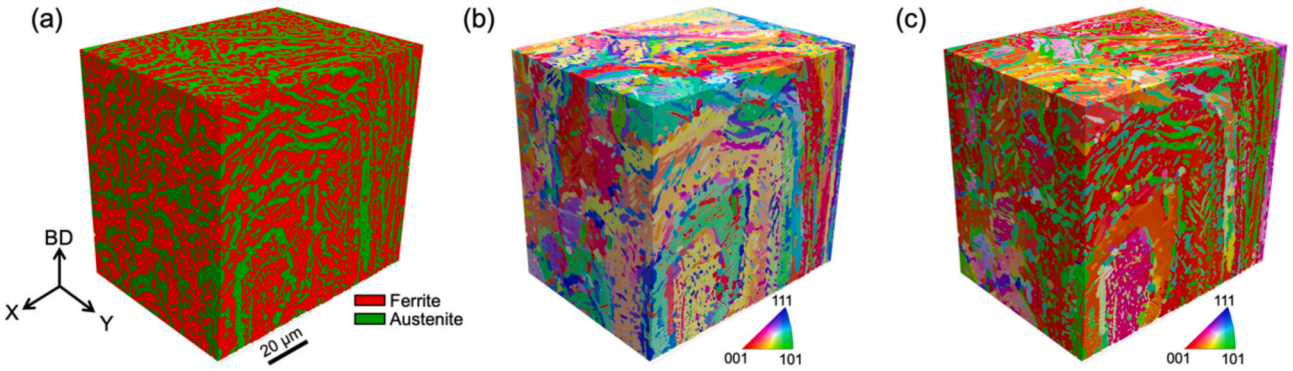

Fig. 3. Overall volumetric views of the microstructure of the thermally treated LPBF DSS 2205. (a) EBSD phase map showing a balanced fraction of ferrite and austenite, BD is along the vertical direction. (b) EBSD IPF map (along Y-direction as shown in coordinate in (a)) displaying columnar grains in the prior ferrite grains alongside fine austenite grains formed during annealing. (c) EBSD IPF map (along BD) indicating a ⟨001⟩//BD texture in ferrite with austenite mainly showing ⟨101⟩//BD texture.

via different ferrite-to-austenite phase transformation pathways.

A complete categorization of ferrite-to-austenite phase transformation pathways is presented in Fig. 4. Austenite grains in EBSD IPF colours along the Y direction are shown for each overall microstructure in Fig. 4(a1) – (d1). Here, different austenite nucleation and growth mechanisms can be observed. Austenite grains nucleated at ferrite-ferrite GBs are identified as intergranular (Fig. 4(a)). Austenite protrusions with no detectable GBs between protrusions and allotriomorphs are further classified as being driven by the instability mechanism (Fig. 4 (b)). In contrast, the austenite protrusions that form a low-angle grain boundary (LAGB) with an intergranular austenite grain are categorized as being formed by sympathetic nucleation (Fig. 4(c)). Lastly, austenite grains that are isolated from any ferrite-ferrite GB and do not form LAGBs with any intergranular austenite are labelled as intragranular (Fig. 4(d)). In this context, it should be noted that EBSD may not be capable of resolving all LAGBs, and the reconstruction process applied to the data excludes all boundaries with disorientations less than 1°. Further, some austenite protrusions may form LAGBs with more than one intergranular austenite grain due to impingement from another austenite grain. This is because the presence of a strong ferrite texture leads to similar orientations among ferrite grains that might translate into similar orientations among austenite grains due to variant selection, similar to what has been reported for titanium alloys undergoing β to α transformation [46]. In this case, when two or more austenite gains grow into each other and impinge, LAGBs may form between them. A sympathetic austenite-austenite interface is therefore defined as the lowest possible misorientation among all LAGBs formed between this protrusion and all neighbouring intergranular austenite grains. Quantitative definitions and criteria of the different austenite types are shown in Fig. 1S(a) in supplementary materials, along with a schematic demonstrating examples for each austenite type with annotations in Fig. 1S(b).

It can be observed that intergranular austenite (Fig. 4(a1)) occupies the greatest volume fraction of all austenite categories, followed by instability-induced austenite (Fig. 4(b1)) which is a sub-category of intergranular austenite. Both sympathetic (Fig. 4(c1)) and intragranular (Fig. 4(d1)) austenite occupy relatively low volume fractions due to their smaller grain sizes. Among all austenite particles, intergranular, sympathetic, and intragranular austenite have a volume fraction of 89 %, 5 %, and 6 %, respectively. Despite their relatively low volume fractions, sympathetic and intragranular austenite are associated with the significant grain refinement in this microstructure after thermal treatment, and play an important role in achieving the optimal combination of mechanical properties as detailed in [27]. Examples of typical grain structures for each austenite category are presented in Fig. 4(a2) – (d2).

3.2. *The characteristics of austenite-ferrite interfaces*

The overall misorientation angle distribution across different types of interfaces is presented in Fig. 5(a). To analyse the interfaces in more depth, they were categorized into two sets, namely austenite-ferrite, and austenite-austenite interfaces. As most of the initial ferrite-ferrite boundaries were consumed by the nucleation and growth of austenite,

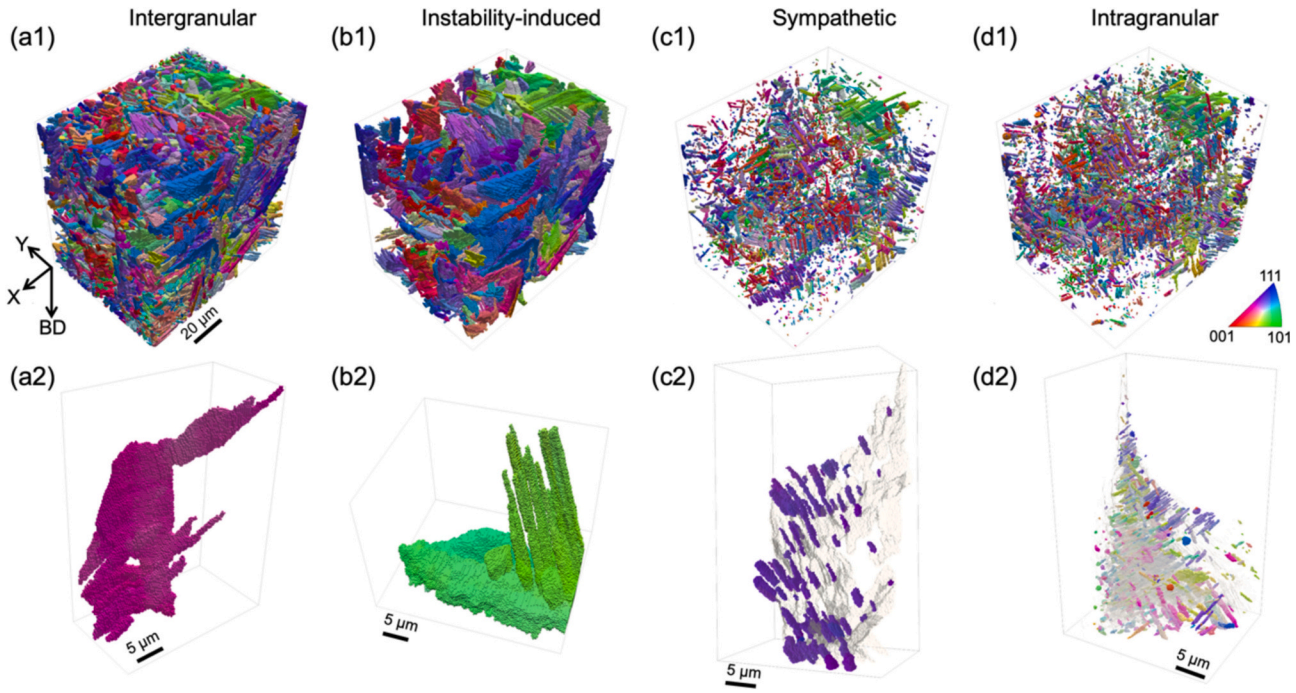

Fig. 4. Austenite categories formed following various ferrite-to-austenite phase transformation pathways presented in 3D EBSD IPF maps along the Y direction. (a) Intergranular, (b) Instability-induced, (c) Sympathetic, and (d) Intragranular austenite shown as (a1) – (d1) overall microstructures in the entire 3D dataset, and (a2) – (d2) typical grain morphologies. (a2) – (b2) are shown in IPF colouring, (c2) sympathetic protrusions are shown in IPF colour, the connecting allotriomorph is shown in semi-transparent light grey, (d2) intragranular particles residing inside the same ferrite grain are shown in IPF colours, the ferrite grain is shown in semi-transparent light grey.

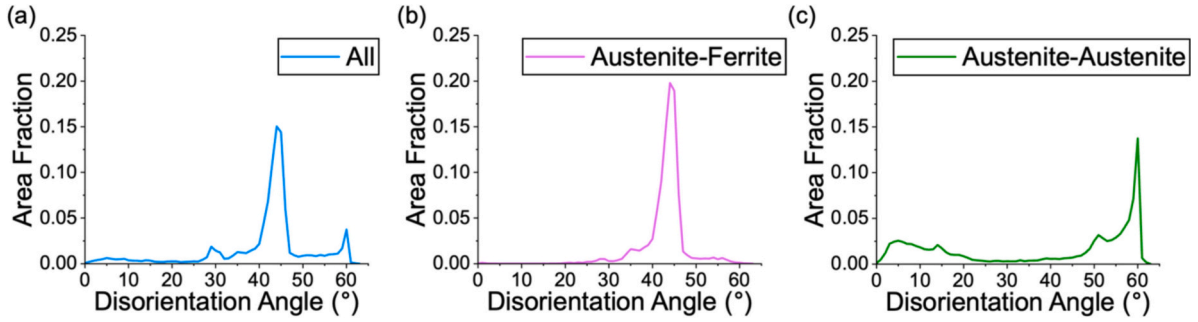

Fig. 5. Misorientation angle distributions for (a) all interfaces (including ferrite-ferrite, austenite-ferrite, and austenite-austenite), (b) austenite-ferrite, and (c) austenite-austenite boundaries in the thermally treated condition.

no further detailed study is carried out on the ferrite-ferrite interfaces due to the limited interface area available, that does not allow for a meaningful conclusion. The misorientation profiles for all boundaries and austenite-ferrite boundaries in Fig. 5(a) and (b) both display a broad peak between 42° and 46° with the entire range spanning from 1° to 62.8°. This points to the potential existence of an OR between austenite and ferrite. It can be determined that the overall misorientation profile of the thermally treated LPBF DSS 2205 is dominated by the austenite-ferrite interfaces, implying that most of the interfaces here are between austenite and ferrite. The misorientation profile for austenite-austenite GBs displayed in Fig. 5(c) exhibits a strong peak at 60°, suggesting the dominance of Σ3 boundaries within austenite grains.

The peak between 42° and 46° in the misorientation angle distributions for the austenite-ferrite interfaces (Fig. 5(b)) matches well with the misorientation angles anticipated for the established orientation relationship (OR) models that describe the BCC to FCC (and reverse) phase transformations. These include Kurdjumov-Sachs (K—S) [47], Nishiyama-Wasserman (N—W) [48], Pitsch (P) [49], Greninger–Troiano

Table 1
Common orientation relationships between FCC austenite and BCC ferrite defined by plane/direction parallelisms and interphase misorientation angle-axis pairs.

Orientation relationship	Parallelism	Angle-axis pair
Pitsch (P) [49]	$\{100\}_{fcc}//\{110\}_{bcc}$ $\langle 110\rangle_{fcc}//\langle 111\rangle_{bcc}$	45.98° ⟨0.08 0.2 0.98⟩

Kurdjumov-Sachs (K—S) [47]	$\{111\}_{fcc}//$
	$\{110\}_{bcc}$
	$\langle 110\rangle_{fcc}//\langle 111\rangle_{bcc}$
		42.85°
		⟨0.968 0.178 0.178⟩

Nishiyama-Wassermann (N—W) [48]	$\{111\}_{fcc}//$
	$\{110\}_{bcc}$
	$\langle 112\rangle_{fcc}//\langle 110\rangle_{bcc}$
		45.98°
		⟨0.976 0.083 0.201⟩

Bain (B) [51]	$\{100\}_{fcc}//$
	$\{100\}_{bcc}$
	$\langle 100\rangle_{fcc}//\langle 110\rangle_{bcc}$
		45°
		⟨100⟩

Greninger-Troiano (G-T) [50]	$\{111\}_{fcc}//$
	$\{110\}_{bcc}$
	$\langle 123\rangle_{fcc}//\langle 133\rangle_{bcc}$
		44.23°
		⟨0.973 0.189 0.133⟩

(G–T) [50], and Bain [51] as summarized in Table 1. Among them, the K—S and N—W ORs are the most versatile models for this phase transformation [13]. For our further study, these interfaces were categorized into three groups, K—S, N—W, and Others, based on misorientation angle and axis pairs. To be eligible for the K—S or N—W classification, the angular deviation from the ideal misorientation angle and axis must be within 5° of that OR. Since the K—S and N—W ORs are only 5.26° apart, the OR with smaller deviation is assigned when the deviation is within 5° for both ORs. All other interfaces are categorized as Others.

Figure 6 presents the overall statistics (Fig. 6(a)) and visualizations (Fig. 6(b) – (d)) of austenite-ferrite interfacial ORs with respect to austenite types including intergranular, sympathetic, and intragranular. From Fig. 6(a), it is obvious that the majority of interphase boundaries are with intergranular austenite, occupying more than 80 % of the total austenite-ferrite boundary area, while sympathetic and intragranular each account for less than 10 % of all interphase boundaries. Despite their relatively low area fractions, the refined sympathetic and intragranular interphase boundaries contribute considerably towards strengthening, by providing extra barriers to dislocation motions during deformation [27]. The K—S OR dominates in all austenite categories. For both sympathetic and intragranular austenite, the interfacial area characterised as having a N—W OR is higher than the one with the Others OR. For intergranular austenite-ferrite interfaces, a significant area fraction belongs to the Others OR while only a small one is assigned the N—W OR. Intergranular austenite possesses 49 % and 10 % of K—S and N—W interfaces, while sympathetic austenite comprises 58 % and 24 % of K—S and N—W interfaces, respectively. Intragranular austenite consists of 53 % and 26 % of K—S and N—W interfaces, respectively. From Fig. 6(b), a high fraction of K—S and Others interfaces are visible alongside a lower fraction of N—W interfaces associated with

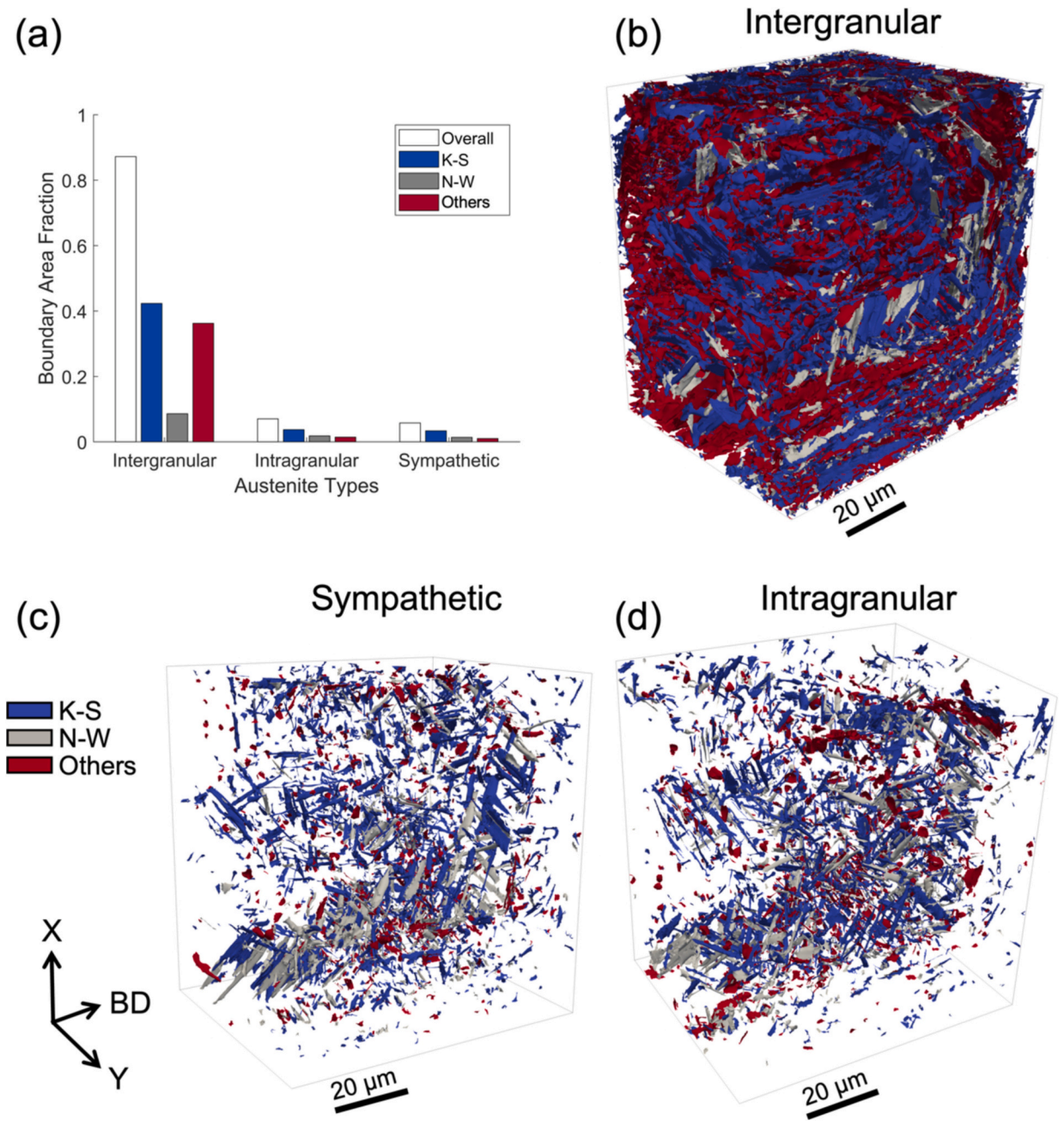

Fig. 6. OR statistics and visualizations. (a) Austenite-ferrite interface area fraction in terms of austenite types and ORs. Visualizations of austenite-ferrite interfaces for (b) intergranular austenite, (c) sympathetic austenite, and (d) intragranular austenite. Colours refer to the type of interface in terms of OR.

intergranular austenite. They are seen to be compact and interpenetrated. Sympathetic (Fig. 6(c)) and intragranular (Fig. 6(d)) austenite share a similar austenite-ferrite interface morphology, involving high fractions of needle shape surfaces with fewer interpenetration and a less compact distribution where K—S is the dominant OR, followed by N—W and Others. K—S and N—W interfaces are known to benefit interphase slip transition between austenite and ferrite during tensile deformation, which contributes to better work-hardening rate for improved mechanical properties [27].

Using the 3D-EBSD data and the method developed in Ref. [17], the interphase habit plane distributions are calculated for the interfaces belonging to intergranular, sympathetic, and intragranular austenite in the reference frames of ferrite (Fig. 7(a) – (c)) and austenite (Fig. 7(d) – (f)). Irrespective of the phase transformation pathway, ferrite and austenite tend to terminate on (110) and (111) planes, respectively. In the case of intergranular, the intensities of (110) ferrite plane and (111) austenite plane are ~1.33 and ~1.67 multiple random distribution (MRD), respectively. For sympathetic and intragranular, the interphase habit plane distributions for ferrite and austenite both exhibit higher intensity than those for the intergranular, with the (110) ferrite plane showing an intensity of ~1.80 RMD and the (111) austenite exhibiting a peak of ~2.10 MRD, respectively.

Using the 3D-EBSD data and the method developed in Ref. [20], the interphase boundary curvature distributions were plotted for the interfaces belonging to intergranular, sympathetic, and intragranular austenite in the reference frames of ferrite (Fig. 8(a) – (c)) and austenite (Fig. 8(d) – (f)). Phase interfaces belonging to intergranular austenite (Fig. 8(a, d)) exhibit much lower curvatures compared to those belonging to sympathetic (Fig. 8(b, e)) and intragranular austenite (Fig. 8(d, f)). An inverse correlation is seen for both ferrite and austenite between the curvature distribution (Fig. 8(a, d)) and the habit plane distribution (Fig. 7(a, d)) for the intergranular transformation path. In the intergranular ferrite lattice frame(Fig. 8(a)), the highest curvatures are located at the (111) plane, corresponding to the planes with the lowest MRD (Fig. 7(a)), while the lowest curvatures on the (110) plane correlate to the highest MRD. Similarly, the highest curvatures in the intergranular austenite lattice frame (Fig. 8(d)) are mostly on the (100) plane, corresponding to the highest MRD (Fig. 7(d)), while the lowest curvatures on the (111) plane correlate to the highest MRD. Although the habit plane distribution and curvature distribution on phase interfaces belonging to sympathetic and intragranular austenite are generally inversely correlated, minor deviations exist. In the sympathetic category, the highest curvatures are located at the (111) plane in the ferrite lattice frame (Fig. 8(b)), whereas the lowest MRD is on the (100) plane (Fig. 7(b)). In the austenite lattice frame, the lowest curvatures on the (110) plane (Fig. 8(e)) also do not match the location of the highest MRD on the (111) plane (Fig. 7(e)). Similar observations in both lattice frames can be made on the intragranular category.

3.2.1. *Intergranular austenite-ferrite interfaces*

Figure 9 shows the interfaces between intergranular austenite and ferrite coloured by unique interface colours. These interfaces are grouped into three categories depending on the austenite-ferrite ORs including K—S (Fig. 9(a) – (b)), N—W (Fig. 9(c) – (d)), and Others (Fig. 9 (e) – (f)), and are displayed from two perspectives (Fig. 9(a, c, e) and Fig. 9(b, d, f)) for better visual representation. Interfaces with a K—S OR between the intergranular austenite and ferrite as seen in Fig. 9(a) – (b) mostly present large boundary areas with a mix of relatively flat, undulating, and needle shaped morphologies. Interfaces with an N—W OR (Fig. 9(c) – (d)) generally exhibit a smaller boundary area compared to that with a K—S OR. They mainly present relatively flat or needle shaped morphologies, with only a few interfaces showing an undulating morphology. Observation of interfaces with an Others OR (Fig. 9(e) – (f)) is similar to what has been described for the ones with a K—S OR, where a mix of relatively flat, undulating, and needle shaped morphologies are seen, primarily with a large boundary area. The undulating morphology is noted less frequently compared to that in the K—S category. Abundant intersections among interfaces are observed in the K—S category, while limited intersections are present in the N—W and Others categories.

The interphase habit plane distributions for the intergranular interfaces classified as K—S, N—W, and Others are shown in the reference frame of ferrite and austenite, respectively in Fig. 10. The ferrite (Fig. 10 (a) – (c)) and austenite ((Fig. 10(d) – (f))) habit planes terminate on (110) and (111) orientations respectively. The K—S (49 % area fraction) and N—W (10 % area fraction) interfaces present stronger intensity in their plane distributions in both lattice frames compared to the Others interfaces (41 % area fraction). The ferrite plane distributions of the

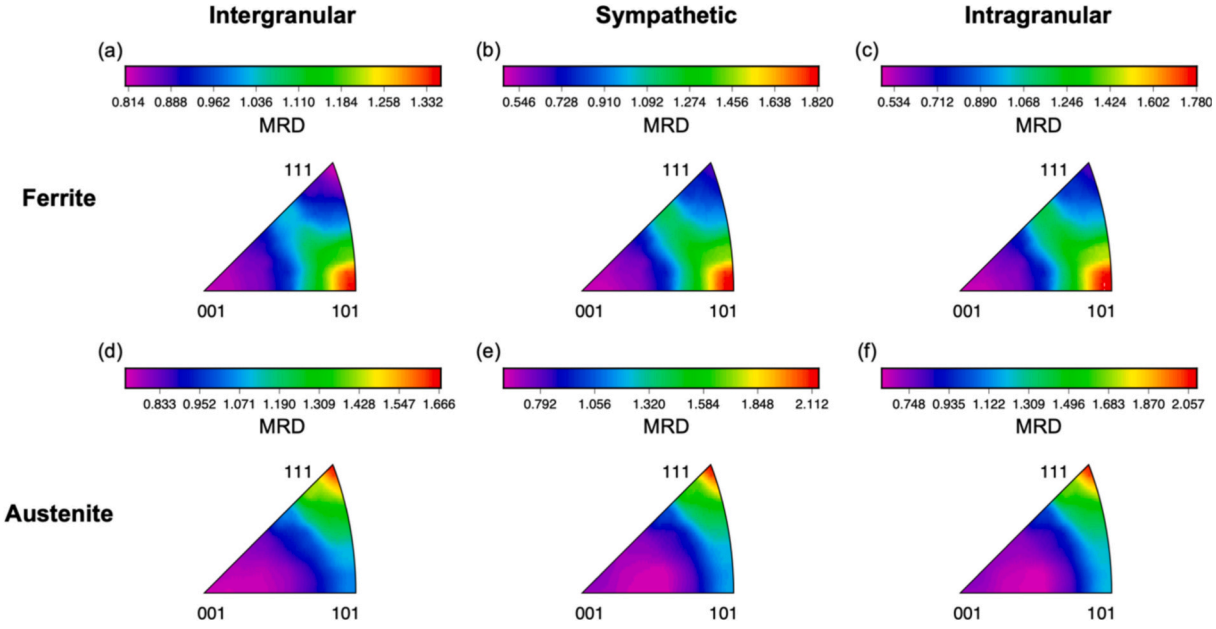

Fig. 7. Grain boundary plane distributions for (a, d) intergranular, (b, e) sympathetic, and (c, f) intragranular austenite-ferrite interfaces in the crystal lattice frames of (a) – (c) ferrite and (d) – (f) austenite. The colour scale represents multiples of random distribution (MRD).

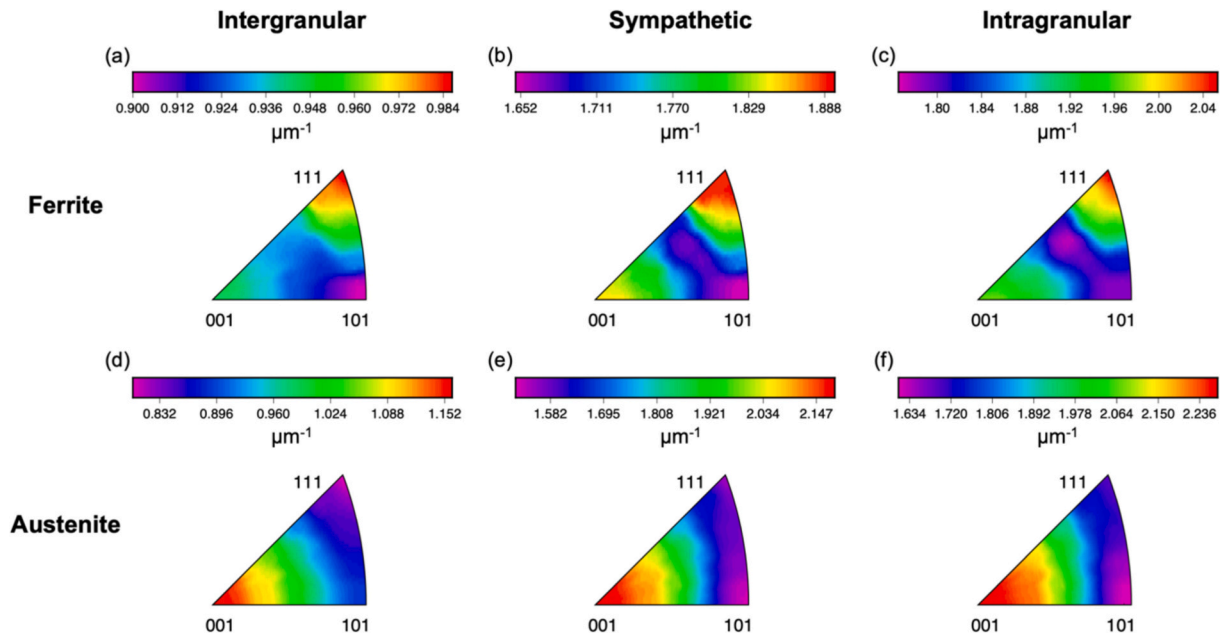

Fig. 8. Grain boundary curvature distributions for (a, d) intergranular, (b, e) sympathetic, and (c, f) intragranular austenite-ferrite interfaces in the crystal lattice frames of (a) – (c) ferrite and (d) – (f) austenite. The colour scale represents curvature in μm^{-1}.

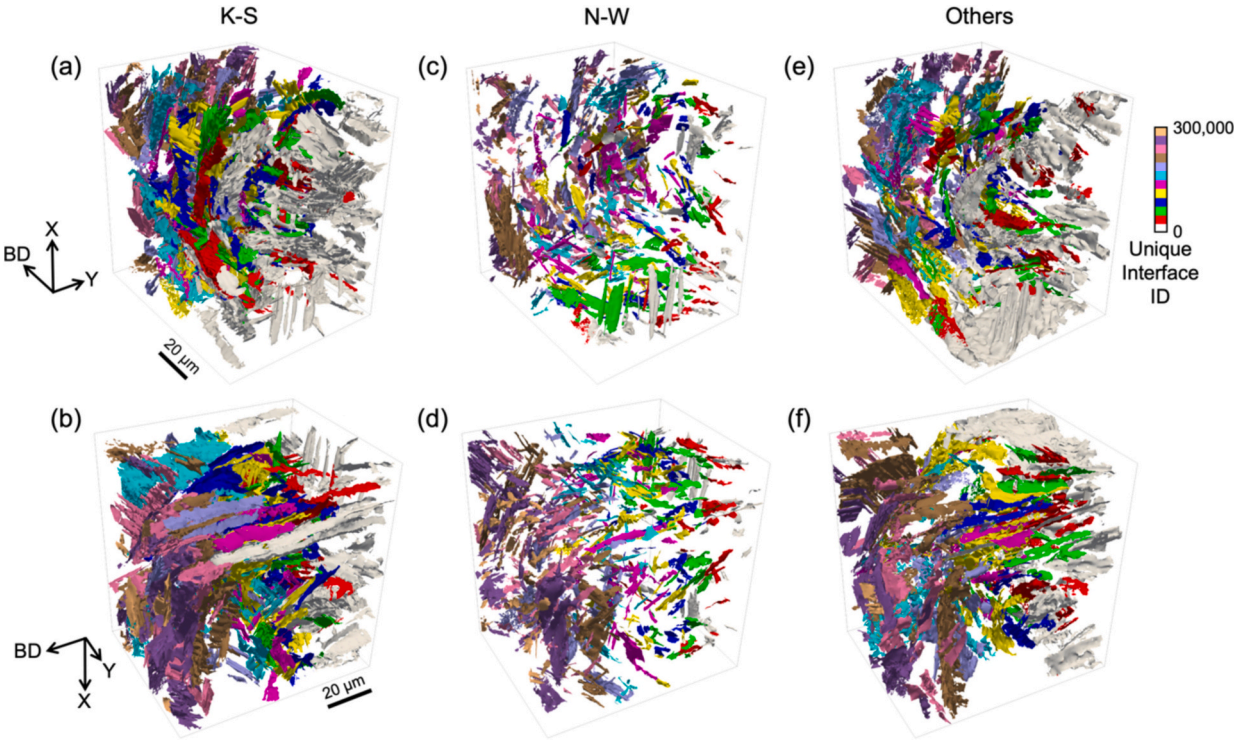

Fig. 9. Visualizations of interfaces between intergranular austenite and ferrite grouped into different ORs including (a) – (b) K—S, (c) – (d) N—W, and (e) – (f) Others, from two different perspectives, (a, c, d), and (b, d, f), respectively. Colours represent unique interface IDs.

K—S and N—W interfaces have maximum intensities of ~1.52 and ~1.58 MRD, respectively, compared to only ~1.10 MRD for that of the Others interfaces. Similarly, the austenite plane distributions of the K—S and N—W interfaces exhibit maximum intensities of ~1.80 and ~1.98 MRD, respectively, compared to ~1.43 MRD for that of the Others interfaces.

The interphase boundary curvature distributions for the intergranular interfaces classified as K—S, N—W, and Others are measured and plotted in the reference frames of ferrite (Fig. 11(a) – (c)) and austenite (Fig. 11(d) – (f)). Generally, an inverse correlation is seen for both ferrite and austenite between the curvature distribution (Fig. 11) and the habit plane distribution (Fig. 10) irrespective of OR. For ferrite, the highest curvatures are at the (100) plane on the K—S interfaces (Fig. 11(a)), associating with the minimal MRDs on the (100) plane (Fig. 10(a)). The highest curvatures are at the (111) ferrite plane for both N—W (Fig. 11 (b)) and Others (Fig. 11(c)) categories, corresponding to their minimal

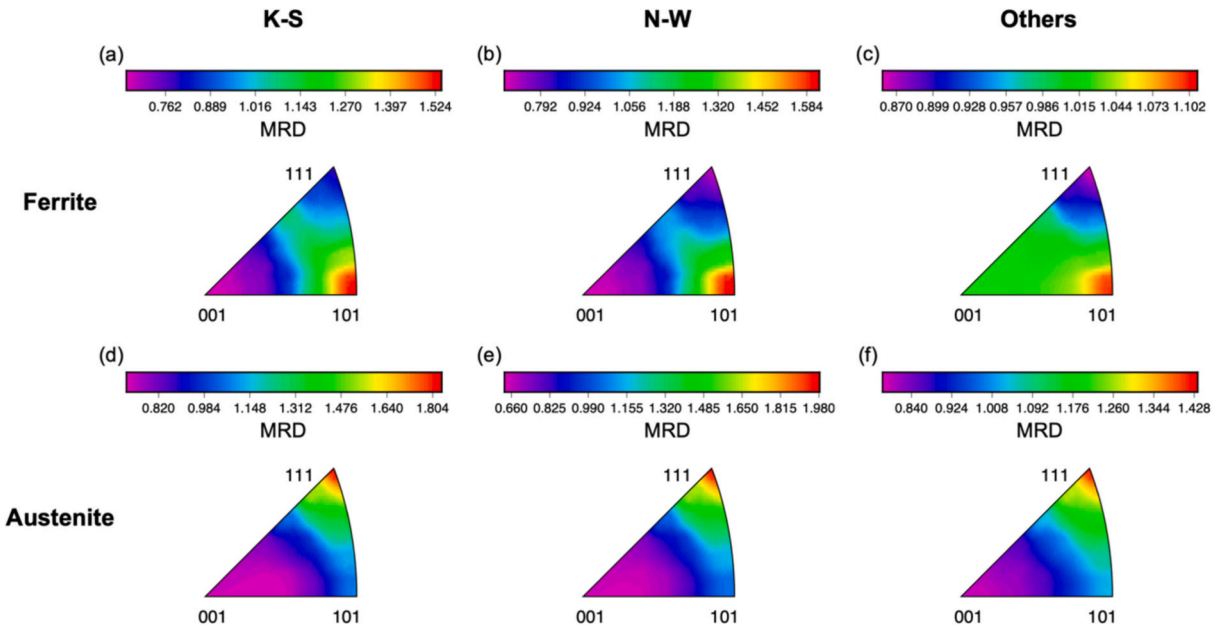

Fig. 10. Grain boundary plane distributions for intergranular austenite-ferrite interfaces in the crystal lattice frames of (a) – (c) ferrite and (d) – (f) austenite, for different ORs of (a, d) K—S, (b, e) N—W and (c, f) Others. The colour scale represents multiples of random distribution (MRD).

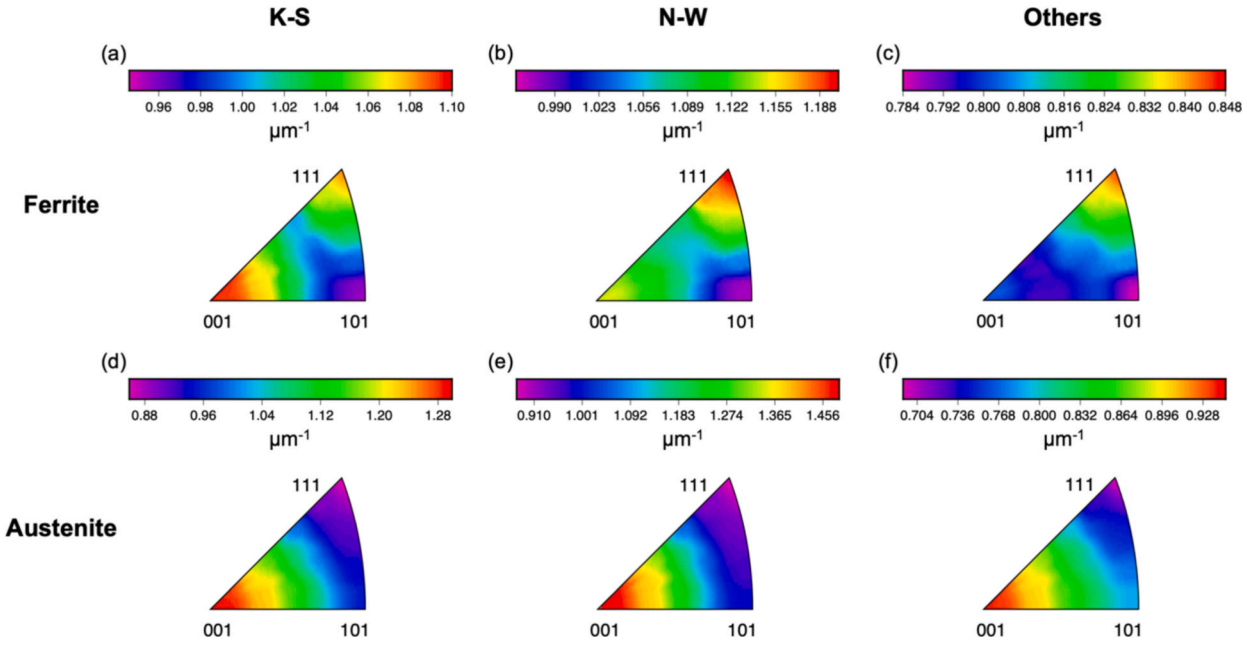

Fig. 11. Grain boundary curvature distributions for intergranular austenite-ferrite interfaces in the crystal lattice frames of (a) – (c) ferrite and (d) – (f) austenite for different ORs of (a, d) K—S, (b, e) N—W and (c, f) Others. The colour scale represents curvature in μm^{-1}.

MRDs on the (111) ferrite plane (Fig. 10(b, c)). The lowest curvatures in the ferrite and austenite lattice frames locate at the (110) and (111) planes, respectively, irrespective of OR, corresponding to the planes with the highest MRDs in their respective plane distributions. The highest austenite curvatures are also positioned on planes with the minimal MRDs, which are at the (100) austenite plane regardless of OR. In both ferrite and austenite reference frames, the intergranular transformation route consistently exhibits the highest curvature (1.19–1.46 μm^{-1}) of interfaces with the N—W OR, followed by the K—S OR (1.10–1.28 μm^{-1}), with the lowest curvature (0.85–0.93 μm^{-1}) observed for interfaces with the Others OR.

3.2.2. *Sympathetic and intragranular austenite-ferrite interfaces*

Figure 12 demonstrate the visualizations of austenite-ferrite interfaces of sympathetic (Fig. 12(a) – (c)) and intragranular austenite (Fig. 12(d) – (f)) respectively, coloured by unique interface colours. These interfaces are grouped into three categories depending on the austenite-ferrite ORs including K—S (Fig. 12(a, d)), N—W (Fig. 12(b, e)), and Others (Fig. 12(c, f)). The needle shaped interfaces are mainly categorized as K-S/N-W (Fig. 12(a, b, d, e)), while the more faceted interfaces mostly belong to Others category (Fig. 12(c, f)). Note that a small number of needle shaped interfaces can be overserved in the Others category for both the sympathetic and the intragranular routes near the sample edge, mostly at the upper right corner. These could be

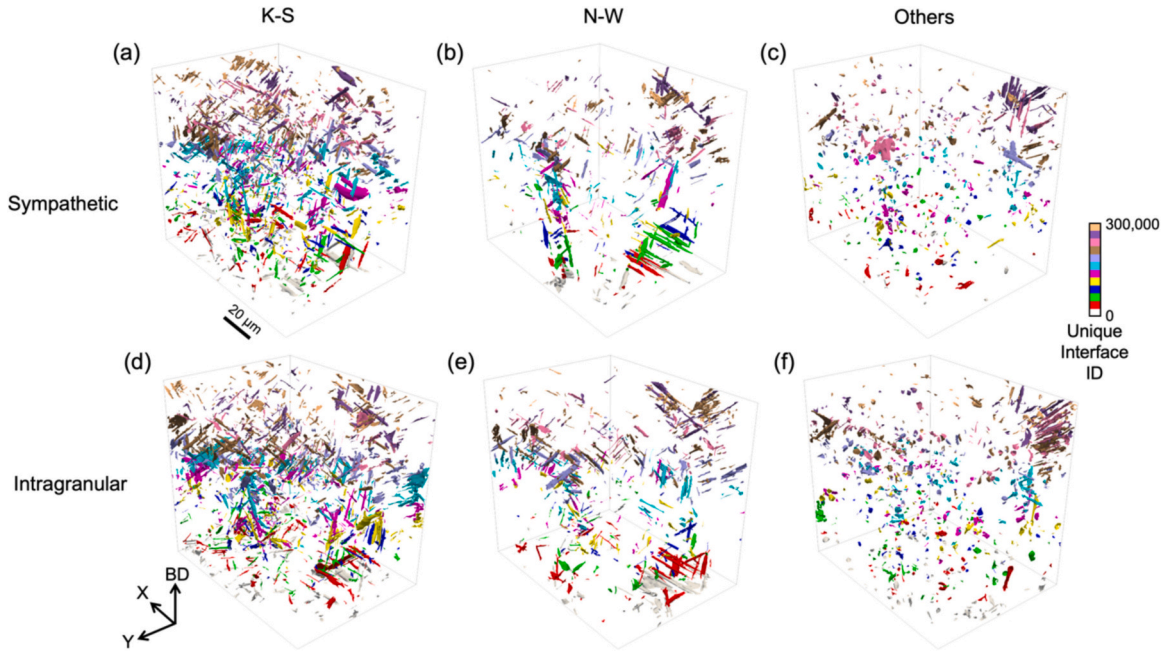

Fig. 12. (a) – (c) Visualizations of austenite-ferrite interfaces of (a) – (c) sympathetic and (d) – (f) intragranular austenite grouped into different ORs including (a, d) K—S, (b, e) N—W, and (c, f) Others. Colours represent unique interface IDs.

the interfaces of the protrusions that are connected to an allotriomorph that is located just beyond the sample edge. Such protrusions that penetrate a ferrite grain located at the sample edges without neighbouring any other ferrite or intergranular austenite are, therefore, falsely classified as intragranular austenite and show their needle shaped interfaces near the sample edge as in Fig. 12(f). On the other hand, these protrusions could coincidently form LAGBs with the intergranular austenite within the sample volume. They are then falsely identified as sympathetic austenite and show their needle shaped interfaces near the sample edge in Fig. 12(c).

The interphase habit plane distributions for sympathetic and intragranular interfaces classified as K—S, N—W, and Others are shown in the reference frame of ferrite (Fig. 13) and austenite (Fig. 14). For both sympathetic and intragranular routes, ferrite terminates on the (110) plane in all OR groups of K—S, N—W, and Others (Fig. 13), where the minimal MRDs are at the (100) plane for the K—S and N—W categories (Fig. 13(a, b)) and (111) plane for the Others category (Fig. 13 (c)). The sympathetic category exhibits stronger peaks (~1.98 MRD) for the N—W OR (Fig. 13(b)) compared to those (Fig. 13(e)) of the intragranular route (~1.80 MRD). In contrast, both sympathetic and intragranular groups present similar intensities at ~1.85 and ~1.17 MRD, respectively, for the K—S (Fig. 13(a, d)) and Others ORs (Fig. 13(c, f)).

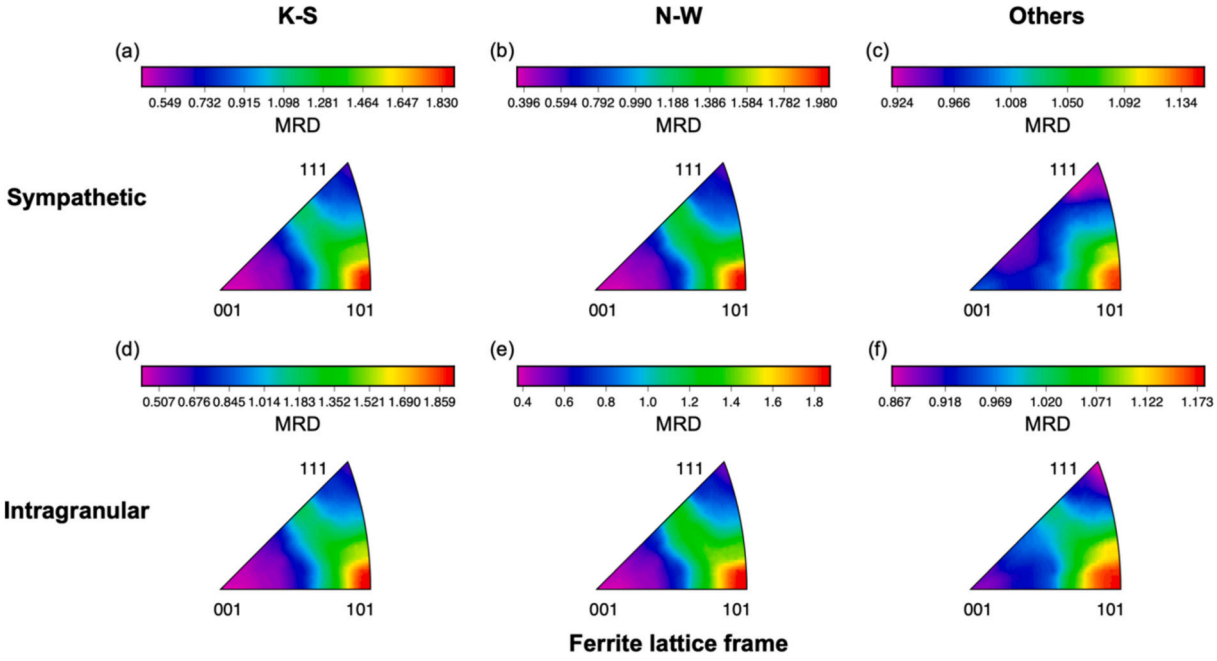

Fig. 13. Grain boundary plane distribution for (a) – (c) sympathetic and (d) – (f) intragranular austenite-ferrite interfaces in the crystal lattice frame of ferrite for different ORs of (a, d) K—S, (b, e) N—W and (c, f) Others. The colour scale represents multiples of random distribution (MRD).

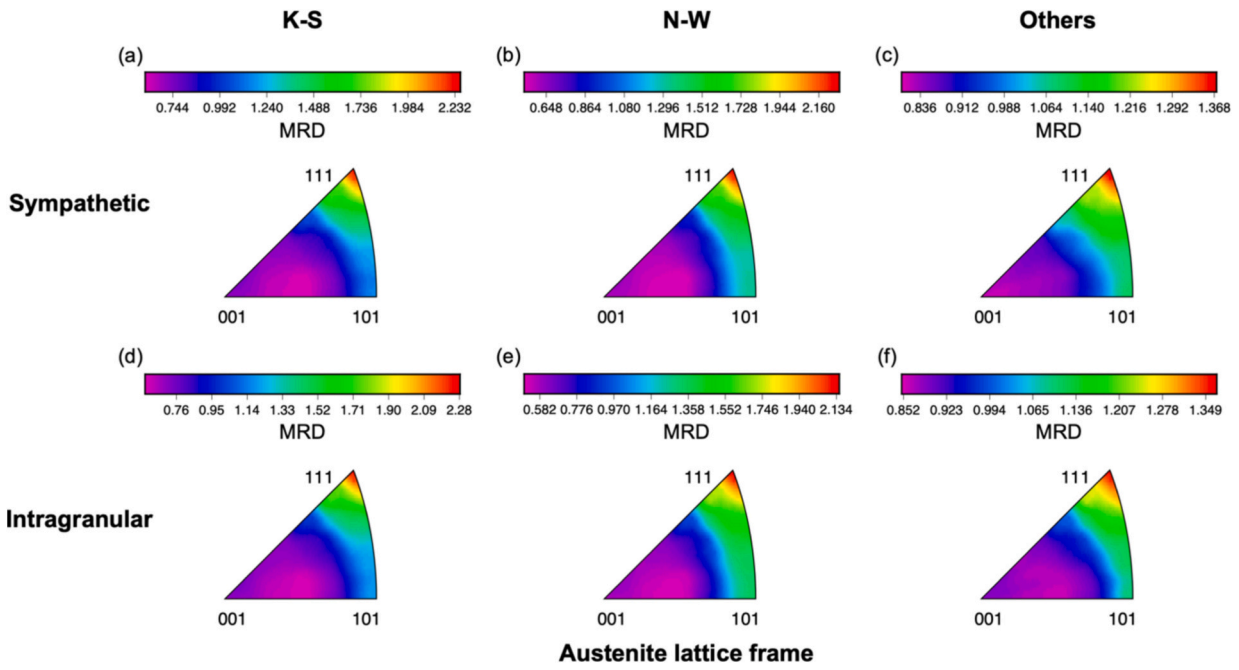

Fig. 14. Grain boundary plane distributions for (a) – (c) sympathetic and (d) – (f) intragranular austenite-ferrite interfaces in the crystal lattice frame of austenite for different ORs of (a, d) K—S, (b, e) N—W and (c, f) Others. The colour scale represents multiples of random distribution (MRD).

The austenite habit plane distributions (Fig. 14) for the sympathetic and intragranular routes all terminate on the (111) plane. The sympathetic and intragranular transformation routes exhibit similar austenite habit plane distribution intensities for the K—S (Fig. 14(a, d)) and N—W OR (Fig. 14(b, e)) categories, where peak intensities around 2.20 MRD are present. The habit plane distribution intensities for the Others OR (Fig. 14(c, f)) in both the sympathetic and intragranular routes (~1.35 MRD) are much lower than those for the K-S/N-W ORs (Fig. 14(a, b, d, e)).

The interphase boundary curvature distributions for sympathetic and intragranular interfaces classified as K—S, N—W, and Others are plotted in the reference frames of ferrite (Fig. 15) and austenite (Fig. 16). In the ferrite lattice frame, an inverse correlation is seen for the K—S category between the curvature distribution (Fig. 15(a, d)) and the habit plane distribution (Fig. 13(a, d)), where the highest curvatures are located at the (100) plane for both sympathetic and intragranular routes, corresponding to the observation that the plane distributions have minimal MRDs on the (100) plane. The lowest ferrite curvatures are also positioned on the (110) plane with maximum MRDs. Overall, the maxima and minima in the curvature (Fig. 15(b, e)) and habit plane distributions (Fig. 13(b, e)) exhibit weaker correlation in the N—W category in the ferrite lattice frame, where the minimal ferrite curvatures deviate

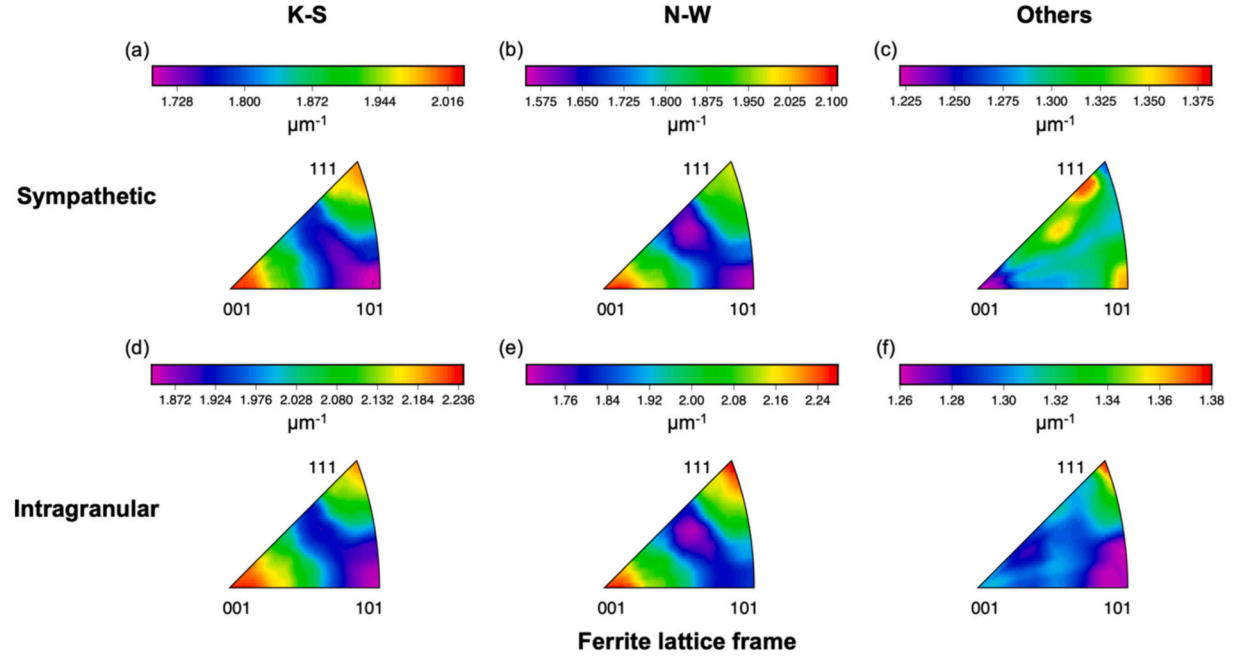

Fig. 15. Grain boundary curvature distributions for (a) – (c) sympathetic and (d) – (f) intragranular austenite-ferrite interfaces in the crystal lattice frame of ferrite for different ORs (a, d) K—S, (b, e) N—W and (c, f) Others. The colour scale represents curvature in μm^{-1}.

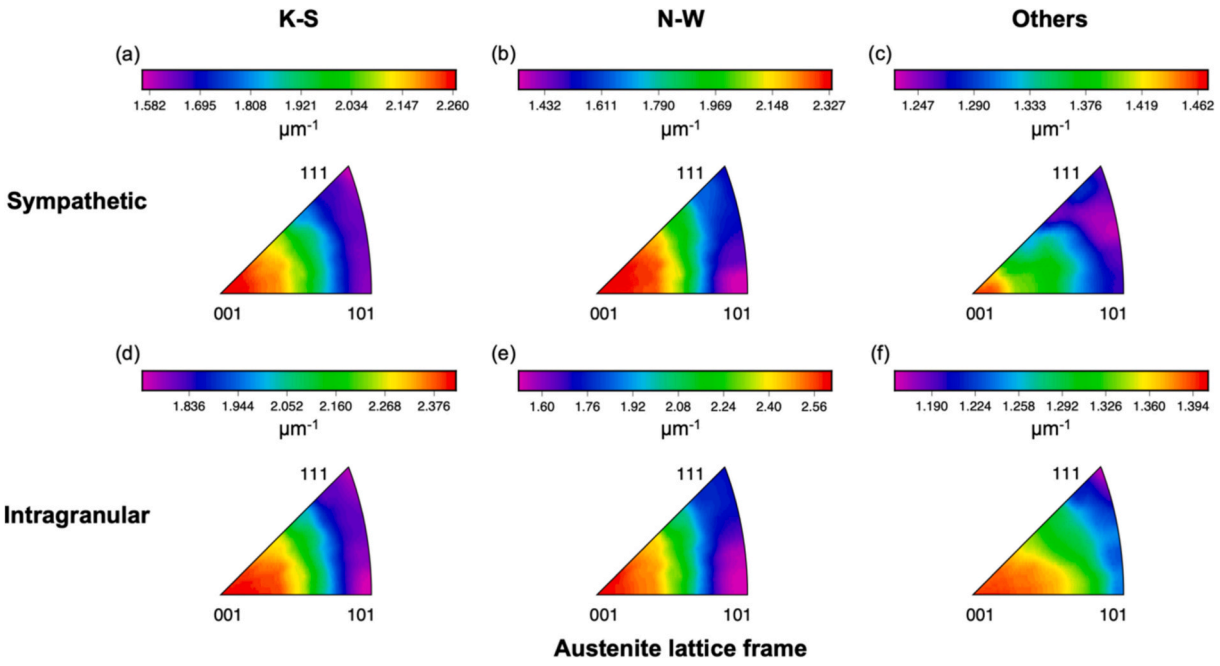

Fig. 16. Grain boundary curvature distributions for (a) – (c) sympathetic and (d) – (f) intragranular austenite-ferrite interfaces in the crystal lattice frame of austenite for different ORs of (a, d) K—S, (b, e) N—W and (c, f) Others. The colour scale represents curvature in μm^{-1}.

from the (110) ferrite plane with maximal MRDs, despite the maximal curvatures are observed on the (100) plane with the minimal MRDs. In the Others category, the ferrite curvature (Fig. 15(f)) and habit plane distributions (Fig. 13(f)) for the intragranular interfaces are inversely correlated, with the maximum and minimum curvatures at the (111) and (110) planes, respectively, matching the minimum and maximum MRDs at the same planes, respectively. In contrast, the ferrite curvature distribution (Fig. 15(c)) for the sympathetic interfaces deviates significantly from an inverse correlation with the habit plane distribution (Fig. 13(c)). The minimum curvatures are at the (100) plane, whereas the maximum MRD is at the (110) plane. Similarly, the location of the maximum curvatures deviates from the (111) plane with the minimum MRD.

In the austenite lattice frame, only the K—S interfaces in the sympathetic route and the Others interfaces in the intragranular route exhibit an inverse correlation between their curvature (Fig. 16(a, f)) and habit plane distributions (Fig. 14(a, f)). Their minimum and maximum curvatures are on the (111) and (100) planes, respectively, corresponding to the maximum and minimum MRDs on the same planes, respectively. For the sympathetic N—W, intragranular K—S, and intragranular N—W interfaces, the minimum curvatures at the (110) austenite plane (Fig. 16(b, d, e)) is not correlated to their maximum MRDs on the (111) plane (Fig. 14(b, d, e)). Similarly, the minimum curvatures of the sympathetic Others interfaces (Fig. 16(c)) also deviate slightly from the (111) plane with the maximum MRD (Fig. 14(c)). In both ferrite and austenite reference frames, both sympathetic and intragranular transformation routes consistently exhibit the highest curvatures (2.33–2.56 μm^{-1}) of interfaces with the N—W OR, followed by ones with the K—S OR (2.26–2.38 μm^{-1}), with the lowest curvatures (~1.4 μm^{-1}) observed for interfaces with the Others OR.

4. Discussion

The current work presents a comprehensive study of the effect of phase transformation pathways on the characteristics of microstructure and interfaces developed during the ferrite-to-austenite phase transformation in a LPBF-processed duplex stainless steel. Building on the detailed characterization enabled by 3D-EBSD, a complete categorization of austenite types based on the transformation path is performed. The results indicate that austenite formed through various phase transformation routes shows different grain structures, interface morphologies, and interface plane and curvature distributions. Considering the impact of austenite morphology and austenite-ferrite interface character on various properties of this class of steels such as deformation mechanisms [27,30], hot working processes [14], and precipitation [15], the current work highlights the significance of phase transformation pathway on the properties of LPBF DSSs. While the focus of this study is on LPBF DSSs, the transformation mechanisms unravelled in 3D can be applied to other AM steels and conventionally manufactured steels that undergo ferrite-to-austenite phase transformations.

4.1. Microstructure characteristics

The phase transformation pathways significantly influence the formation mechanisms of the various types of austenite formed. An ultrafine morphology of austenite is achieved in the LPBF DSS 2205 upon thermal treatment followed by water quenching. The microstructure mainly consists of allotriomorphic, instability-induced, sympathetic, and intragranular austenite. During the ferrite-to-austenite phase transformation, elastic strain is introduced once the lattice change occurs. The phase transformation can only proceed further if the elastic strain is relaxed. Being held at 1000 °C for 10 min, the phase transformation is assumed to progress through a diffusional process [13].

The intragranular austenite may be formed by heterogeneous nucleation on inclusions [13], dislocations, or at the intersection of substructures (e.g., sub-boundaries) [52]. Different mechanisms have been suggested to explain the formation of austenite protrusions from the allotriomorphic morphology, including preferential growth of austenite along the ferrite sub-structures [52], sympathetic nucleation [53,54], and the instability mechanism [52,55]. Here, the first mechanism is possible due to the high density of dislocations in the as-built microstructure induced by LPBF thermal cycles as shown in Fig. 2(d). The categorization of sympathetic protrusions (Fig. 4(c)) with a low-angle austenite-austenite boundary where the misorientation is between 1° and 15° suggest abundant sympathetic nucleation of austenite. On the other hand, the observation of many protrusions without austenite-

austenite boundary (Fig. 4(b)) is consistent with the instability mechanism. This advocates the contribution of both sympathetic nucleation and instability mechanisms to producing the abundant protrusions.

4.2. Interface characteristics

The phase transformation pathways significantly affect the characteristics of austenite-ferrite interfaces as underpinned by our experimental data. This is associated with the thermal history during and post-LPBF, as well as the distinct phase transformation mechanisms for different types of austenite.

The phase transformation pathway (i.e., austenite category) drastically affects the population of K—S and N—W austenite-ferrite interfaces. For instance, sympathetic and intragranular austenite present a significantly higher fraction of K-S/N-W (82 % and 79 %, respectively) interfaces compared to intergranular austenite (58 %). Austenite preferentially nucleates and grows along the prior ferrite-ferrite grain boundaries, forming intergranular austenite, where different interface configurations could potentially form on different sides of the boundaries depending on the thermal condition. The possible austenite nuclei interfaces can be summarised into three configurations, including: (i) rational interfaces with all neighbouring ferrite grains; (ii) rational interface(s) with only one or two ferrite grains, and (iii) irrational interfaces with all neighbouring ferrite grains. The high undercooling (due to high cooling rate) during LPBF [1,3,4] mainly encourages the development of austenite nuclei with rational interfaces (type (i) and (ii)), while the type (iii) interfaces are primarily formed during lower undercooling (lower cooling rate) and/or isothermal holding [56,57]. During the post-LPBF thermal treatment, the phase transformation occurs at 1000 °C. In such a high temperature regime, the energy barrier for austenite nucleation with an irrational or rational interface is not significantly different compared to that at lower temperatures. Hence, the formation of both interfaces is possible, leading to interfaces that do not fulfill the K-S/N-W ORs. This may assist the development of austenite nuclei with Others (non-KS/NW) interface characteristics on intergranular austenite. Nevertheless, most of the intergranular austenite nuclei are formed during LPBF, which leads to the majority of allotriomorphic austenite still obeying configuration (i) or (ii). In addition, when austenite forms at a prior ferrite-ferrite GB, it may not hold K-S/N-W ORs with different ferrite grains on different sides, unless the orientation of theses ferrite grains are very similar. This then leads to a high fraction of intergranular austenite nuclei that formed during LPBF with configuration (ii), adding to the area fraction of the Others OR to a value that is close to that of the K—S OR (Fig. 6(a)).

The austenite-ferrite interface characteristics as well as the austenite morphology are determined by the phase transformation pathway. Ferrite-ferrite GBs could be the most desirable nucleation and growth sites for austenite [58], where the allotriomorphic austenite initially nucleates during LPBF at high undercooling. Subsequently, the allotriomorphic austenite nuclei continue to grow while new nuclei start to form along other ferrite-ferrite boundaries during post-LPBF isothermal annealing, enabling formation of large allotriomorphic grains. The resulting phase boundary could be partially coherent with both the rationally and irrationally orientated neighbouring ferrite grains and, hence, contain misfit-compensating defects [59,60]. These defects could encourage the sympathetic nucleation of austenite on existing austenite allotriomorphs. Concomitantly, austenite-ferrite interface perturbation could occur, leading to the development of instability-induced austenite. On the other hand, the diffusivity of substitutional and/or interstitial atoms could be influenced by lattice defects such as dislocations since the planar density of atoms may be lowered by the defects and generate additional free volumes that could become desirable pathways for atomic diffusion [61].

In other words, the strain and the high dislocation density resulted from LPBF accelerates elemental diffusion and, thus, phase transformations [61,62]. This leads to preferential transformation on ferrite dislocation structures, and ultimately, substantial directional growth of austenite along the K-S/N-W interfaces. This enables the nucleation and growth of intragranular austenite protrusions and contributes to the further directional growth of sympathetic austenite protrusions that had already nucleated on austenite allotriomorphs. In addition, incoherent inclusion such as Si—O also assist austenite nucleation and growth, resulting in dispersed non-directional growth without any specific ferrite-austenite OR [58]. This leads to the non-KS/NW interfaces of intragranular austenite as well as the non-KS/NW growth of sympathetic austenite that had already nucleated on austenite allotriomorphs. Such energetically unfavourable OR decelerates austenite growth and leads to the relatively small interfacial areas (Fig. 12(c, f)). Hence, most interphase interfaces on the sympathetic (82 % area fraction) and intragranular austenite (79 % area fraction) obey the K-S/N-W ORs, as opposed to the relatively large area fraction of non-KS/NW interfaces on the intergranular austenite, including allotriomorph and instability categories. However, most K-S/N-W interfaces are still on intergranular austenite as shown in Fig. 6(a), owing to the usually larger austenite-ferrite interface area on the allotriomorphic austenite.

Among the interfaces examined, K—S is a more prevalent OR compared to N—W in all austenite categories. One reason could be that the K—S OR preserves the original KS misorientation when austenite goes through twinning during growth [13]. In contrast, this is not feasible following the N—W OR [63]. It should be noted that the existence of local chemical heterogeneities is unavoidable during a phase transformation, which may induce a local deviation of the interface from its ideal OR. It has also been shown that minor misalignment with the ideal rational OR may yield a better balance between the energy minimization in the interface and the overall atom matching [64].

The current study demonstrates that habit planes for ferrite and austenite mostly terminate on (110) and (111) planes, respectively (Figs. 7, 10, 13, 14). Termination of ferrite and austenite on (110) and (111) planes, respectively, is crystallographically favoured based on the interfacial parallelism developed during the phase transformation. These planes also have the highest coordination numbers, and closely match the prediction made according to Near-Coincidence Site geometrical matching of FCC-BCC lattices [65–67]. The peak at these planes can also be explained by the first nearest neighbour broken bond model, inferring a minimum plane energy at (110) and (111) planes for BCC and FCC crystal structures, respectively [68].

It should be noted that a lower curvature (i.e., flatter interface) is correlated with a lower grain boundary energy when a constant mean field chemical potential is assumed following [20]. Meanwhile, in a microstructure where grain growth is driven by interfacial grain boundary energy minimization, the grain boundary energy distribution is frequently reported to have an inverse correlation with the grain boundary plane distribution [69–71]. This is the case so that lower-energy boundaries are more populated than higher-energy boundaries to minimize the system energy. This leads to the expectation that an inverse correlation between plane and curvature distributions will exist if grain growth is primarily motivated by interfacial energy minimization.

For intergranular austenite, curvature distributions (Fig. 11) are correlated with the habit plane distributions (Fig. 10) in both ferrite and austenite, where minimal curvatures are generally observed in the planes with maximum relative areas. This observation suggests that austenite nucleation and growth on parent ferrite-ferrite GBs are predominantly controlled by grain boundary energy minimization. The lower curvatures observed in the Others category compared to those of K-S/N-W may be attributed to the formation of type (ii) interface configuration on the intergranular austenite-ferrite interfaces. This often involves a relatively large and flat interface on the austenite allotriomorph that does not fulfill the K-S/N-W ORs. Hence, those flat non-KS/NW interfaces on the allotriomorph leads to a lower curvature in the Others category.

Sympathetic and intragranular transformation routes demonstrate

partially non-correlating grain boundary plane and curvature distributions both in general (Fig. 7(b, c, e, f), Fig. 8(b, c, e, f)) and under different ORs (Fig. 13(b, c, e), Fig. 14(b, c, d, e), Fig. 15(b, c, e), Fig. 16 (b, c, d, e)). Furthermore, they also present similar interface morphologies under the K—S, N—W, and Others categories respectively (Fig. 12), along with their similar area fractions of K-S/N-W interfaces. Additionally, they also present similar grain structures (Fig. 4(c1, d1)). The heterogeneous nucleation theory has been reported for both sympathetic [72] and intragranular austenite [13]. The heterogeneous nucleation and growth of austenite is reported to occur on ferrite substructures such as sub-boundaries [52]. In a proeutectoid ferrite transformation, precipitates or inclusions dispersed in the parent austenite grains are recognized to be the heterogeneous nucleation sites for intragranular ferrite [58,73]. Although the effects of ferrite sub-boundaries can mostly be ruled out here since the grain boundary criteria is set to 1° in the current dataset, hence, most of the sub-boundaries (1~15°) are identified as grain boundaries. In turn, the presence of non-equilibrium microstructures including dislocations and inclusions in ferrite due to the rapid cooling rate and thermal cycling during LPBF could play an important role in influencing the nucleation and growth of the sympathetic and intragranular austenite here. For heterogeneous nucleation on dislocations, transformation strain is effectively accommodated by the strain field of dislocations [58].

In a titanium alloy, autocatalytic nucleation, a similar phenomenon to sympathetic nucleation, was reported to be motivated by strain energy instead of interfacial energy [74]. Here, for sympathetic and intragranular transformation routes, the majority of curvature distributions (Fig. 15, Fig. 16) show only partially inverse correlation with the habit plane distributions (Fig. 13, Fig. 14) as minimal curvatures are in most cases not observed on the planes with maximal MRDs. In addition, both ferrite and austenite habit planes experience higher curvature on the K—S and N—W interfaces (Fig. 15(a, b, d, e), Fig. 16(a, b, d, e)) compared to that on the non-KS/NW interfaces (Fig. 15(c, f), Fig. 16(c, f)). K—S and N—W ORs are generally associated with lower interfacial energy [75] and lower grain boundary energy is usually correlated with lower curvature (i.e., flatter interface) [20]. The unexpected trend observed in the sympathetic and intragranular austenite here indicates that interfacial energy minimization may not be the only driving force for the ferrite-austenite interfaces in the current microstructure with substantial protrusion growth. Strain energy minimization by nucleation on existing dislocations and inclusions could also be an important factor controlling the phase transformation pathways for sympathetic and intragranular austenite. This strain accommodation dictated by the existing ferrite sub-structures ultimately leads to the diffuse ferrite habit plane distribution and the non-correlating grain boundary plane and curvature distributions in both the ferrite and austenite lattice frames.

In iron-carbon steels, where the solid-state phase transformation proceeds from austenite to α-ferrite, sympathetic nucleation was recognized to occur when an α-ferrite nucleus develops at the interface between a pre-existing α-ferrite grain and the parent γ-austenite phase [54,72]. Similarly, the sympathetic austenite in the current study could have first nucleated on a pre-existing austenite, at the interface between this austenite and the parent ferrite phase, and the subsequent growth of the sympathetic austenite could be assisted by the existing ferrite substructure, as also supported by the heterogenous nucleation theory [72]. Sympathetic growth involves the formation of a LAGB between the pre-existing austenite and the sympathetic austenite, which inevitably increases the interfacial energy between the two austenite grains. Therefore, a higher fraction of K-S/N-W interfaces in the sympathetic transformation route (82 %) compared to that in the intragranular one (79 %), which also undergoes heterogeneous nucleation and growth on ferrite sub-structures, could be attributed to the need to minimize the interfacial energy via obeying the rational K-S/N-W ORs, so that the combined strain and interfacial energy can be minimized.

5. Conclusions

In the current work, the effects of the phase transformation pathways on the characteristics of microstructure and interfaces developed during the δ-ferrite to austenite phase transformation were systematically studied using 3D orientation data. New insights provided can facilitate duplex microstructure design using additive manufacturing and post-processing to unlock superior properties. In addition, the transformation mechanisms revealed in 3D can also be applied to other AM steels and conventionally fabricated steels that experience ferrite-to-austenite phase transformation. The main findings are summarised below:

1. The δ-ferrite-to-austenite solid-state phase transformation in a LPBF DSS 2205 leads to development of different types of austenite classified based on formation mechanisms, namely intergranular, instability-induced, intragranular, and sympathetic austenite.
2. Intergranular austenite occupies the highest grain volume and ferrite-austenite interfacial area among all types of austenite due to the typically large grain size of allotriomorph austenite. Intergranular austenite also accounts for most non-KS/NW interfaces since allotriomorph austenite tends to obey K-S/N-W ORs with only one of the neighbouring ferrite grains, and instability-induced growth due to interface perturbation may not necessarily obey any specific OR.
3. Regardless of phase transformation route and OR, ferrite and austenite terminate on the expected (110) and (111) planes, respectively. These planes are both crystallographically and energetically favourable.
4. The ferrite and austenite on the intergranular ferrite-austenite interfaces tends to obey the expected inverse correlation between the plane and curvature distributions. In contrast, the ferrite and austenite on the sympathetic and intragranular ferrite-austenite interfaces exhibits partially non-correlating plane and curvature distributions under different ORs, as minimal curvatures are in most cases not observed on the planes with maximal MRDs.
5. Sympathetic and intragranular austenite display a much higher fraction of K-S/N-W interfaces compared to intergranular austenite. This is because their subsequent growth along existing ferrite dislocations favours the formation of rational phase interfaces.
6. Sympathetic and intragranular austenite exhibit similar grain structures, interface morphologies, K-S/N-W interface fractions, and grain boundary plane distributions. This is associated to their formation via heterogeneous nucleation on existing austenite and dislocation structures, respectively.
7. The formation of an LAGB between sympathetic austenite and intergranular austenite is associated with a slightly higher K-S/N-W interface area fraction in the sympathetic route compared to the intragranular route, even though both transformation routes possess similar grain and interface characteristics. This is driven by systematic energy minimization considering both strain energy and interfacial energy. Hence, there is a greater need to minimize the interfacial energy during further sympathetic growth by obeying the K-S/N-W ORs. This is because the formation of an LAGB at the time of nucleation already increases the interfacial energy compared to the absence of LAGB in intragranular formation.
8. Observation of lower curvature values for non-KS/NW interfaces in sympathetic and intragranular austenite supports the argument that the driving force for their microstructure development during phase transformation is a combination of strain energy and interfacial energy minimization.

Using 3D-EBSD coupled with grain boundary crystallography, the different austenite types and interfaces formed in a DSS 2205 during post-LPBF thermal treatment were unambiguously classified. This clarifies various ferrite-to-austenite phase transformation pathways driven by different mechanisms, controlling the characteristics of austenite

grains and phase interfaces. These are linked to the non-equilibrium microstructures in the predominantly ferritic as-LPBF condition. Since grain structure and interface characteristics substantially influence materials properties, these new insights help inform microstructure design using AM.

CRediT authorship contribution statement

X.Y. He: Writing – original draft, Methodology, Investigation, Formal analysis, Data curation, Conceptualization. **Z.P. Xu:** Writing – review & editing, Formal analysis, Data curation. **G.S. Rohrer:** Writing – review & editing, Formal analysis, Data curation. **C. Kong:** Writing – review & editing, Formal analysis, Data curation. **S. Primig:** Writing – review & editing, Supervision, Methodology, Funding acquisition, Conceptualization. **N. Haghdadi:** Writing – review & editing, Supervision, Methodology, Funding acquisition, Conceptualization.

Declaration of competing interest

The authors declare that they have no known competing financial interests or personal relationships that could have appeared to influence the work reported in this paper.

Acknowledgements

Funding from the AUSMURI program administered by the Australia's Department of Industry, Science, Energy and Resources is acknowledged. S. Primig and N. Haghdadi are supported by the Australian Research Council Discovery program (DP230101063). The authors acknowledge the facilities, scientific, and technical support provided at the Electron Microscope Unit, UNSW Sydney (Mark Wainwright Analytical Centre), a node of Microscopy Australia, a national research facility supported under the Commonwealth NCRIS program.

Appendix A. Supplementary data

Supplementary data to this article can be found online at https://doi.org/10.1016/j.matchar.2025.114745.

Data availability

Data will be made available on request.

References

[1] D. Herzog, V. Seyda, E. Wycisk, C. Emmelmann, Additive manufacturing of metals, Acta Mater. 117 (2016) 371–392, https://doi.org/10.1016/j.actamat.2016.07.019.
[2] N. Haghdadi, M. Laleh, M. Moyle, S. Primig, Additive manufacturing of steels: a review of achievements and challenges, J. Mater. Sci. 56 (2021) 64–107.
[3] X. He, H. Wang, Z. Zhu, L. Wang, J. Liu, N. Haghdadi, S. Nai, J. Huang, S. Primig, S. Ringer, X. Liao, Texture evolution in a CrMnFeCoNi high-entropy alloy manufactured by laser powder bed fusion, J. Mater. Sci. 57 (21) (2022) 9714–9725.
[4] D. Gu, Y.-C. Hagedorn, W. Meiners, G. Meng, R.J.S. Batista, K. Wissenbach, R. Poprawe, Densification behavior, microstructure evolution, and wear performance of selective laser melting processed commercially pure titanium, Acta Mater. 60 (9) (2012) 3849–3860.
[5] M. Das, V.K. Balla, D. Basu, S. Bose, A. Bandyopadhyay, Laser processing of SiC-particle-reinforced coating on titanium, Scr. Mater. 63 (4) (2010) 438–441.
[6] N. Haghdadi, C. Ledermueller, H. Chen, Z. Chen, Q. Liu, X. Li, G. Rohrer, X. Liao, S. Ringer, S. Primig, Evolution of microstructure and mechanical properties in 2205 duplex stainless steels during additive manufacturing and heat treatment, Mater. Sci. Eng. A 835 (2022), https://doi.org/10.1016/j.msea.2022.142695.
[7] F. Hengsbach, P. Koppa, K. Duschik, M.J. Holzweissig, M. Burns, J. Nellesen, W. Tillmann, T. Tröster, K.-P. Hoyer, M. Schaper, Duplex stainless steel fabricated by selective laser melting - microstructural and mechanical properties, Mater. Des. 133 (2017) 136–142, https://doi.org/10.1016/j.matdes.2017.07.046.
[8] M. Alnajjar, F. Christien, K. Wolski, C. Bosch, Evidence of austenite by-passing in a stainless steel obtained from laser melting additive manufacturing, Addit. Manuf. 25 (2019) 187–195, https://doi.org/10.1016/j.addma.2018.11.004.
[9] R. DeMott, N. Haghdadi, X. Liao, S.P. Ringer, S. Primig, 3D characterization of microstructural evolution and variant selection in additively manufactured Ti-6Al-4 V, J. Mater. Sci. 56 (26) (2021) 14763–14782.
[10] R. DeMott, N. Haghdadi, Z. Gandomkar, X. Liao, S. Ringer, S. Primig, Formation and 3D morphology of interconnected α microstructures in additively manufactured Ti-6Al-4V, Materialia 20 (2021) 101201.
[11] R. DeMott, P. Collins, C. Kong, X. Liao, S. Ringer, S. Primig, 3D electron backscatter diffraction study of α lath morphology in additively manufactured Ti-6Al-4V, Ultramicroscopy 218 (2020) 113073.
[12] X. Wan, H. Wang, L. Cheng, K. Wu, The formation mechanisms of interlocked microstructures in low-carbon high-strength steel weld metals, Mater. Charact. 67 (2012) 41–51.
[13] N. Haghdadi, P. Cizek, P.D. Hodgson, V. Tari, G.S. Rohrer, H. Beladi, Effect of ferrite-to-austenite phase transformation path on the interface crystallographic character distributions in a duplex stainless steel, Acta Mater. 145 (2018) 196–209, https://doi.org/10.1016/j.actamat.2017.11.057.
[14] N. Haghdadi, P. Cizek, H. Beladi, P. Hodgson, Dynamic restoration processes in a 23Cr-6Ni-3Mo duplex stainless steel: effect of austenite morphology and interface characteristics, Metall. Mater. Trans. A 48 (2017) 4803–4820.
[15] N. Haghdadi, D. Abou-Ras, P. Cizek, P. Hodgson, A. Rollett, H. Beladi, Austenite-ferrite interface crystallography dependence of sigma phase precipitation using the five-parameter characterization approach, Mater. Lett. 196 (2017) 264–268.
[16] C.M. Hefferan, J. Lind, S.F. Li, U. Lienert, A.D. Rollett, R.M. Suter, Observation of recovery and recrystallization in high-purity aluminum measured with forward modeling analysis of high-energy diffraction microscopy, Acta Mater. 60 (10) (2012) 4311–4318.
[17] M.N. Kelly, K. Glowinski, N.T. Nuhfer, G.S. Rohrer, The five parameter grain boundary character distribution of α-Ti determined from three-dimensional orientation data, Acta Mater. 111 (2016) 22–30.
[18] Z. Sun, S.-P. Tsai, P. Konijnenberg, J.-Y. Wang, S. Zaefferer, A large-volume 3D EBSD study on additively manufactured 316L stainless steel, Scr. Mater. 238 (2024) 115723.
[19] F. Papillon, G.S. Rohrer, P. Wynblatt, Effect of segregating impurities on the grain-boundary character distribution of magnesium oxide, J. Am. Ceram. Soc. 92 (12) (2009) 3044–3051.
[20] X. Zhong, D.J. Rowenhorst, H. Beladi, G.S. Rohrer, The five-parameter grain boundary curvature distribution in an austenitic and ferritic steel, Acta Mater. 123 (2017) 136–145.
[21] C.-S. Kim, A.D. Rollett, G.S. Rohrer, Grain boundary planes: new dimensions in the grain boundary character distribution, Scr. Mater. 54 (6) (2006) 1005–1009.
[22] T. Watanabe, Grain boundary engineering: historical perspective and future prospects, J. Mater. Sci. 46 (12) (2011) 4095–4115.
[23] T. Sun, B. Yao, A.P. Warren, K. Barmak, M.F. Toney, R.E. Peale, K.R. Coffey, Surface and grain-boundary scattering in nanometric cu films, Phys. Rev. B 81 (15) (2010) 155454.
[24] T. Searles, J. Tiley, A. Tanner, R. Williams, B. Rollins, E. Lee, S. Kar, R. Banerjee, H. Fraser, Rapid characterization of titanium microstructural features for specific modelling of mechanical properties, Meas. Sci. Technol. 16 (1) (2004) 60.
[25] S. Motomura, T. Hara, T. Omori, R. Kainuma, M. Nishida, Morphological and chemical analysis of bainite in cu–17Al–11Mn (at.%) alloys by using orthogonal FIB-SEM and double-EDS STEM, J. Electron Microsc. 65 (3) (2016) 243–252.
[26] R. DeMott, N. Haghdadi, C. Kong, Z. Gandomkar, M. Kenney, P. Collins, S. Primig, 3D electron backscatter diffraction characterization of fine α titanium microstructures: collection, reconstruction, and analysis methods, Ultramicroscopy 230 (2021) 113394.
[27] X. He, H. Wang, X. Liao, S. Ringer, N. Haghdadi, S. Primig, Nano-twining and deformation-induced martensitic transformation in a duplex stainless steel 2205 fabricated by laser powder bed fusion, Addit. Manuf. 84 (2024) 104110.
[28] R. Gunn, Duplex Stainless Steels: Microstructure, Properties and Applications, Woodhead Publishing, 1997.
[29] K. Tsuzaki, H. Matsuyama, M. Nagao, T. Maki, High-strain rate superplasticity and role of dynamic recrystallization in a superplastic duplex stainless steel, Mater. Trans. JIM 31 (11) (1990) 983–994.
[30] B. Verhaeghe, F. Louchet, B. Doisneau-Cottignies, Y. Bréchet, J.-P. Massoud, Micromechanisms of deformation of an austenoferritic duplex stainless steel, Philos. Mag. A 76 (5) (1997) 1079–1091.
[31] N. Haghdadi, H. Chen, Z. Chen, S.S. Babu, X. Liao, S.P. Ringer, S. Primig, Intergranular precipitation and chemical fluctuations in an additively manufactured 2205 duplex stainless steel, Scr. Mater. 219 (2022) 114894.
[32] N. Haghdadi, A. Breen, H. Chen, F. Theska, W. Davids, X. Liao, G. Rohrer, S. Ringer, S. Primig, New insights into the character of austenite-ferrite boundaries in an additively manufactured duplex stainless steel, Scr. Mater. 245 (2024) 116049.
[33] D. Zhang, A. Liu, B. Yin, P. Wen, Additive manufacturing of duplex stainless steels - a critical review, J. Manuf. Process. 73 (2022) 496–517, https://doi.org/10.1016/j.jmapro.2021.11.036.
[34] A. Iams, J. Keist, T. Palmer, Formation of austenite in additively manufactured and post-processed duplex stainless steel alloys, Metall. Mater. Trans. A 51 (2) (2020) 982–999.
[35] M.A. Valiente Bermejo, K. Thalavai Pandian, B. Axelsson, E. Harati, A. Kisielewicz, L. Karlsson, Microstructure of laser metal deposited duplex stainless steel: influence of shielding gas and heat treatment, Weld. World 65 (3) (2021) 525–541.
[36] J.-H. Wen, L.-J. Zhang, J. Ning, F. Xue, X.-W. Lei, J.-X. Zhang, S.-J. Na, Laser additively manufactured intensive dual-phase steels and their microstructures, properties and corrosion resistance, Mater. Des. 192 (2020) 108710.

[37] N. Haghdadi, M. Laleh, H. Chen, Z. Chen, C. Ledermueller, X. Liao, S. Ringer, S. Primig, On the pitting corrosion of 2205 duplex stainless steel produced by laser powder bed fusion additive manufacturing in the as-built and post-processed conditions, Mater. Des. 212 (2021), https://doi.org/10.1016/j.matdes.2021.110260.
[38] L. Giannuzzi, N. Smith, TEM specimen preparation with plasma FIB Xe+ ions, Microsc. Microanal. 17 (S2) (2011) 646–647.
[39] M.A. Groeber, M.A. Jackson, DREAM.3D: a digital representation environment for the analysis of microstructure in 3D. Integrating materials and manufacturing, Innovation 3 (1) (2014) 56–72, https://doi.org/10.1186/2193-9772-3-5.
[40] F. Bachmann, R. Hielscher, H. Schaeben, Texture analysis with MTEX – free and open source software toolbox, Solid State Phenom. 160 (2010) 63–68, https://doi.org/10.4028/www.scientific.net/SSP.160.63.
[41] U. Ayachit, The paraview guide: a parallel visualization application, Kitware, Inc, 2015.
[42] M. Groeber, S. Ghosh, M.D. Uchic, D.M. Dimiduk, A framework for automated analysis and simulation of 3D polycrystalline microstructures.: part 1: statistical characterization, Acta Mater. 56 (6) (2008) 1257–1273.
[43] S. Ghosh, Y. Bhandari, M. Groeber, CAD-based reconstruction of 3D polycrystalline alloy microstructures from FIB generated serial sections, Comput. Aided Des. 40 (3) (2008) 293–310.
[44] J. Goldfeather, V. Interrante, A novel cubic-order algorithm for approximating principal direction vectors, ACM Transact. Graphics (TOG) 23 (1) (2004) 45–63.
[45] D. Rowenhorst, A. Lewis, G. Spanos, Three-dimensional analysis of grain topology and interface curvature in a β-titanium alloy, Acta Mater. 58 (16) (2010) 5511–5519.
[46] Z. Zhao, Q. Wang, Q. Hu, J. Liu, B. Yu, R. Yang, Effect of β (110) texture intensity on α-variant selection and microstructure morphology during β→ α phase transformation in near α titanium alloy, Acta Mater. 126 (2017) 372–382.
[47] G. Kurdjumov, G. Sachs, Over the mechanisms of steel hardening, Z. Phys. 64 (325–343) (1930).
[48] Z. Nishiyama, X-ray investigation of the mechanism of the transformation from face centered cubic lattice to body centered cubic, Sci. Rep. Tohoku Univ. 23 (1934) 637.
[49] W. Pitsch, Der orientierungszusammenhang zwischen zementit und austenit, Acta Metall. 10 (9) (1962) 897–900.
[50] A.B. Greninger, A.R. Troiano, The mechanism of martensite formation, Jom 1 (1949) 590–598.
[51] E.C. Bain, N. Dunkirk, The nature of martensite, Trans. AIME 70 (1) (1924) 25–47.
[52] D. Phelan, R. Dippenaar, Instability of the delta-ferrite/austenite interface in low carbon steels: the influence of delta-ferrite recovery sub-structures, ISIJ Int. 44 (2) (2004) 414–421.
[53] C. Chen, H. Yen, J. Yang, Sympathetic nucleation of austenite in a Fe–22Cr–5Ni duplex stainless steel, Scr. Mater. 56 (8) (2007) 673–676.
[54] D. Phelan, R. Dippenaar, Widmanstätten ferrite plate formation in low-carbon steels, Metall. Mater. Trans. A 35 (2004) 3701–3706.
[55] W.W. Mullins, R.F. Sekerka, Morphological stability of a particle growing by diffusion or heat flow, J. Appl. Phys. 34 (2) (1963) 323–329.
[56] W.B. Hutchinson, L. Ryde, P.S. Bate, Transformation textures in steels, in: Materials Science Forum, Trans Tech Publ, 2005, pp. 1141–1150.
[57] Y. Adachi, K. Hakata, K. Tsuzaki, Crystallographic analysis of grain boundary bcc-precipitates in a Ni–Cr alloy by FESEM/EBSD and TEM/Kikuchi line methods, Mater. Sci. Eng. A 412 (1–2) (2005) 252–263.
[58] T. Furuhara, T. Maki, Variant selection in heterogeneous nucleation on defects in diffusional phase transformation and precipitation, Mater. Sci. Eng. A 312 (1–2) (2001) 145–154.
[59] T. Furuhara, J. Howe, H. Aaronson, Interphase boundary structures of intragranular proeutectoid α plates in a hypoeutectoid Ti-Cr alloy, Acta Metall. Mater. 39 (11) (1991) 2873–2886.
[60] J.F. Nie, B.C. Muddle, T. Furuhara, H.I. Aaronson, Toward the overthrow of half of a major paradigm for interfacial structure deduction, with special attention to the massive transformation in Ti-46.5 A/O Al alloy, Scr. Mater. 39 (4-5):637-645 (1998).
[61] L. Zhao, N. Park, Y. Tian, A. Shibata, N. Tsuji, Deformation-assisted diffusion for the enhanced kinetics of dynamic phase transformation, Mater. Res. Lett. 6 (11) (2018) 641–647.
[62] M. Biglari Jr., E. Mittemeijer, Simulation of the massive austenite–ferrite transformation under uniaxial loading, Comput. Mater. Sci. 77 (2013) 214–223.
[63] J.J. Jonas, Y. He, G. Langelaan, The rotation axes and angles involved in the formation of self-accommodating plates of Widmanstätten ferrite, Acta Mater. 72 (2014) 13–21.
[64] C. Shek, J. Lai, K. Wong, C. Dong, Early-stage widmanstatten growth of the γ phase in a duplex steel, Metall. Mater. Trans. A 31 (2000) 15–19.
[65] Q. Liang, W. Reynolds, Determining interphase boundary orientations from near-coincidence sites, Metall. Mater. Trans. A 29 (1998) 2059–2072.
[66] T. Furuhara, T. Maki, K. Oishi, Interphase boundary structure with irrational orientation relationship formed in grain boundary precipitation, Metall. Mater. Trans. A 33 (2002) 2327–2335.
[67] G. Miyamoto, R. Hori, B. Poorganji, T. Furuhara, Crystallographic analysis of proeutectoid ferrite/austenite interface and interphase precipitation of vanadium carbide in medium-carbon steel, Metall. Mater. Trans. A 44 (2013) 3436–3443.
[68] J. Mackenzie, A. Moore, J. Nicholas, Bonds broken at atomically flat crystal surfaces—I: face-centred and body-centred cubic crystals, J. Phys. Chem. Solids 23 (3) (1962) 185–196.
[69] J. Gruber, D.C. George, A.P. Kuprat, G.S. Rohrer, A.D. Rollett, Effect of anisotropic grain boundary properties on grain boundary plane distributions during grain growth, Scr. Mater. 53 (3) (2005) 351–355.
[70] D.M. Saylor, A. Morawiec, G.S. Rohrer, Distribution of grain boundaries in magnesia as a function of five macroscopic parameters, Acta Mater. 51 (13) (2003) 3663–3674.
[71] D.M. Saylor, A. Morawiec, G.S. Rohrer, The relative free energies of grain boundaries in magnesia as a function of five macroscopic parameters, Acta Mater. 51 (13) (2003) 3675–3686.
[72] H. Aaronson, G. Spanos, R. Masamura, R. Vardiman, D. Moon, E. Menon, M. Hall, Sympathetic nucleation: an overview, Mater. Sci. Eng. B 32 (3) (1995) 107–123.
[73] S. Mizoguchi, J. Takamura, Proc. 6th Int. Iron and Steel Cong, ISIJ Tokyo, 1990.
[74] B. Radhakrishnan, S. Gorti, S.S. Babu, Phase field simulations of autocatalytic formation of alpha lamellar colonies in Ti-6Al-4V, Metall. Mater. Trans. A 47 (2016) 6577–6592.
[75] Y.-J. Zhang, G. Miyamoto, K. Shinbo, T. Furuhara, Effects of α/γ orientation relationship on VC interphase precipitation in low-carbon steels, Scr. Mater. 69 (1) (2013) 17–20.